A Mechanistic Basis for Inhibition of TREK-2 K2P Channels by Norfluoxetine

Peter Proks [1, 2], Marcus Schewe [3], Linus J. Conrad [1,2], Shanlin Rao [4],

Kristin Rathje [3], Karin E. J. Rödström[5], Elisabeth P. Carpenter [2,5],

Thomas Baukrowitz [3], and Stephen J Tucker [1, 2]*

[1] Clarendon Laboratory, Department of Physics, University of Oxford, Oxford, UK;

[2] OXION Initiative in Ion Channels and Disease, University of Oxford, Oxford, UK;

[3] Department of Physiology, University of Kiel, Kiel, Germany;

[4] Department of Biochemistry, University of Oxford, Oxford, UK;

[5] Centre for Medicines Discovery, University of Oxford, UK.

**All correspondence should be addressed to: stephen.tucker@physics.ox.ac.uk*

Key Words: *K2P channel, KCNK10, TREK-2, Norfluoxetine; ML335; K^+ channel gating*

ABSTRACT

The TREK subfamily of Two-Pore Domain (K2P) K^+ channels are inhibited by low micromolar concentrations of fluoxetine and its metabolite, norfluoxetine (NFx). Although not the principal target of this antidepressant, TREK channel inhibition by NFx has provided important insights into the conformational changes associated with channel gating and highlighted the role of the selectivity filter in this process. Yet despite the availability of TREK-2 crystal structures with NFx bound, the precise mechanisms which underlie NFx inhibition remain elusive. Such investigations ideally require examining the effects of the drug on single channel behavior. However, wild-type TREK channels normally exhibit a very low open probability which makes analysis of their inhibition at the single channel level extremely challenging. In this study, we show how the unique behavior of single TREK-2 channels reconstituted in lipid bilayers can be used to study NFx inhibition in detail. Our results reveal the primary mechanism of NFx inhibition is a complex allosteric process that results in both a reduced open probability and single channel conductance. Furthermore, we show the transduction mechanism involved in NFx inhibition can be disrupted by the action of ML335, and can also be subject to desensitization. We also uncover several voltage-dependent effects of NFx inhibition. In addition, we propose a gating scheme that accounts these effects and which provide important insights into the action of agonists and antagonists on K2P channel function.

Introduction

Within the Two-Pore domain (K2P) family of K^+ channels, the TREK subfamily (TREK-1, TREK-2, and TRAAK) are regulated by a diverse array of chemical and physical stimuli that couple different cellular and environmental signals to changes in cellular electrical activity (Enyedi and Czirjak, 2010; Niemeyer et al., 2016). TREK channels are located throughout the central and peripheral nervous system where they are involved in variety of processes including mechanosensation, thermosensation and nociception (Djillani et al., 2019a). As a consequence of their apparent role in these tissues, selective TREK channel agonists have been proposed as potential analgesics (Vivier et al., 2016) (Mathie and Veale, 2015) and several inhibitors are also considered possible antidepressants (Heurteaux et al., 2006; Djillani et al., 2019b). Understanding the mechanisms by which such small molecules and other compounds modulate TREK channel activity is therefore important to fully realize their therapeutic potential.

In a previous study we solved crystal structures of the human TREK-2 channel in two distinct conformations known as the 'up' and 'down' conformations (Dong et al., 2015). In that same study, we also determined structures of TREK-2 in complex with two known inhibitors, namely fluoxetine and its active metabolite, norfluoxetine (NFx). Fluoxetine (Prozac™) is a commonly prescribed antidepressant and although its principal action as a selective serotonin reuptake inhibitor is well characterized, its inhibitory effects on TREK channels remain of interest due to the reported link between TREK-1 and depression and the fact it is one of the few relatively high-affinity blockers of TREK channels currently available (Kennard et al., 2005; Heurteaux et al., 2006). Furthermore, the crystal structures revealed that NFx binds within the side fenestrations of the channel formed by a gap between the transmembrane (TM) domains; consequently, the NFx binding site is only available in the down state because these gaps are not present in the up state. The ability to use NFx as a probe to distinguish between these two conformational states not only revealed that both up and down states represent functionally conductive conformations (McClenaghan et al., 2016), but also helped develop structural models for TREK-2 activation by membrane stretch (Aryal et al., 2017; Clausen et al., 2017). However, the precise mechanism by which NFx binding within the fenestrations leads to an inhibition of TREK channel activity remains unclear.

Although the TASK-1 K2P channel possesses a lower 'X-gate' analogous to the classical helix bundle-crossing found in many other K^+ channels(Rodstrom et al., 2020), most K2P channels, including TREK channels, do not have a lower gate. Instead they appear to gate primarily within their selectivity filter (Bagriantsev et al., 2011; Piechotta et al., 2011; Rapedius et al., 2012; Schewe et al., 2016). Current models for TREK channel gating propose that movement

of the TM helices influences this filter gating mechanism, but does not restrict access to the inner cavity of the channel.

There are a number of possible mechanisms by which NFx binding within the pore may influence TREK channel gating; these range from direct block of the pore by NFx and/or electrostatic effects of its positively charged amine on K^+ permeation, to more complex allosteric effects of bound NFx on movement of the channel from the down to up conformation, as well as possible allosteric effects of NFx binding on the selectivity filter gate itself. The ability of NFx to impair movement from the down to up conformation has been demonstrated (Dong et al., 2015; Aryal et al., 2017), but it also known that this is unlikely to fully explain the inhibitory effects of NFx (McClenaghan et al., 2016). The relative importance of these various mechanisms therefore remains unknown.

In this study we have examined the inhibition of TREK-2 channel activity by NFx in detail at both the macroscopic and single channel level. Our results indicate that inhibition appears to be primarily via allosteric effects on the selectivity filter gate and we provide a kinetic model for the intrinsic states of this gate that provides important new insight into the effects of different agonists and antagonists on selectivity filter gating in ion channels.

Results and Discussion

Direct effects of NFx on TREK-2 gating. Quaternary ammonium (QA) ions such as Tetrapentylammonium (TPA) are known to bind to a variety of K^+ channels deep within the cavity just below the selectivity filter, and have proven useful tools of in the study of channel pore structure and gating (Armstrong, 1971; Baukrowitz and Yellen, 1996; Piechotta et al., 2011). In TREK-2, the two binding sites for NFx are also located below the selectivity filter and although not directly below the entrance to the filter, these sites are close enough to overlap with the central binding site for TPA (**Figure 1A,B**) (Dong et al., 2015). Such overlapping sites are therefore predicted to result in direct competition between these ligands and so we examined whether NFx inhibition of TREK-2 was affected by the presence of TPA.

Figure 1C shows NFx produces concentration-dependent inhibitory effects in giant inside-out patches excised from *Xenopus* oocytes expressing wild-type (WT) human TREK-2. The IC_{50} for channel inhibition was ~3 μM at physiological pH7.4. However, when similar dose-response curves were measured in the presence of 80 μM TPA there was a marked reduction in the efficacy of NFx inhibition (IC_{50} to ~65 μM; **Figure 1D**). Importantly, there was little shift in NFx inhibition with the smaller sized QA, Tetraelthylammonium (TEA) which is not predicted

to overlap with the NFx binding site (**Figure 1D**). A recent crystal structure also reveals the binding site for BL1249, a TREK channel activator, overlaps with both NFx and the larger QA ion, Tetrahexylammonium (THexA) (Schewe et al., 2019). Consistent with a direct physical interaction between these compounds, a reduced activatory effect of BL1249 was observed in the presence NFx, and THexA (**Figure 1E**).

Non-competitive antagonism of NFx inhibition by TREK-2 activators. Recent crystal structures show that another TREK-2 agonist, ML335 binds to a site behind the selectivity filter that is also distant from the NFx binding site and not predicted to overlap (Lolicato et al., 2017). Interestingly, we still observed a marked reduction in the NFx inhibition in the presence of 50 μM ML335 (IC_{50} increased from ~3 to ~160 μM; **Figure 1F,G**). This effect appears specific as activation by another agonist, 2-aminoethoxydiphenyl borate (2-APB), whose binding site is also is not predicted to overlap (Zhuo et al., 2015) had little effect on NFx inhibition (**Figure 1G**).

It has been proposed that ML335 binding just behind the selectivity filter directly activates the filter gating mechanism by changing the dynamic flexibility of the pore loops (Lolicato et al., 2020). The antagonistic effect of ML335 we observe on NFx inhibition therefore suggests that NFx may also inhibit via this filter gating mechanism. However, it is difficult to exclude other possible effects of NFx based upon macroscopic recordings alone, and so to gain further insight we next examined the effects NFx inhibition on the behavior of TREK-2 at the single channel level.

Characterization of TREK-2 single channel behavior. Detailed analysis of the effect of drugs on single channel behavior can provide important insights into the mechanism of drug action. However, there are two major problems when applying this to the study of wild-type TREK2 and its inhibition by NFx. The first problem stems from the variable kinetics and conductances reported for wild-type TREK-2 single channels (Kang et al., 2007). These are thought to arise from the multiple isoforms produced by alternative translation initiation sites within the N-terminus (Simkin et al., 2008), but irrespective of the cause, this complicates analysis of single channel data. The second issue is that, unless they are activated, individual TREK-2 channels have a very low 'resting' open probability (P_o) which also makes analyzing the effects of an inhibitor extremely difficult.

However, in a previous study we measured the activity of individual TREK-2 channel proteins reconstituted into a lipid bilayer (Clausen et al., 2017). These purified proteins are the same as those used to obtain crystal structures of TREK-2 with and without NFx bound (Dong et al., 2015), and although truncated at both the N- and C-termini, they still produce functional channels that can be activated by various agonists such as BL1249 and ML335, and also

retain their ability to be inhibited by NFx (Dong et al., 2015; Lolicato et al., 2017). Importantly, these single-protein species channels in bilayers do not exhibit the variable single channel conductances reported for WT TREK2 expressed in heterologous systems and so we chose to examine the effects of NFx on recordings of single TREK-2 channels recorded in this system.

Characterization of single TREK-2 channels in lipid bilayers. Regardless of their orientation in the bilayer, we found that the P_o of most reconstituted TREK channels was strongly voltage-dependent with inward currents having much lower P_o than outward currents (**Figure 2A**). This "standard" behavior results in outwardly-rectifying macroscopic currents similar to those observed in many previous recordings of TREK-2 currents (**Figure 2B**). But we also found that the P_o of these channels was often not stationary over long periods of time meaning that detailed analysis of NFx inhibition would be challenging.

However, in ~10% of recordings, TREK-2 was observed to exhibit a high P_O mode of behavior for both outward and inward currents (**Figure 2C**) which resulted in a quasi-symmetrical current-voltage relationship (**Figure 2D**). Interestingly, if several channels were present in a recording, they would all exhibit either the "standard" or "high P_o" mode of gating but were never observed together. The conformational identity of this high P_o gating mode is unknown, but, as described further on, it retains NFx sensitivity indicating that it cannot be the 'up' state as this lacks the fenestration binding sites for NFx. Instead it may simply reflect the ability of the channel to adopt more than one functionally open state whilst in the 'down' conformation (McClenaghan et al., 2016). Either way, the high P_o of these channels and their stability over long periods of time made them particularly suitable for analysis of single-channel kinetics and the effects of inhibitors such as NFx.

We therefore examined the kinetics of these channels in more detail; the distributions of openings of both inward (-60 mV) and outward (+60 mV) currents in both standard and high P_o mode were well-fitted by a single exponential (**Supplementary Figure S2**). The mean open time in the high P_o mode at +60 mV (P_o =0.90±0.04; n=7) was 4.9±1.4 ms (n=7). In the standard mode (mean P_o =0.32±0.25; n=10), the corresponding mean open time was significantly lower: 1.4±0.6 ms (n=10; $p<0.001$). Interestingly, in contrast to the mean open time of the outward currents which rose sharply above P_o of 0.8, the mean open time of the inward currents at -60 mV showed no obvious dependency on P_o (**Supplementary Figure S1**). This suggests the gating of inward and outward currents may be governed by different open states.

The distribution of closings of both inward and outward TREK-2 channels in the standard mode were well fit by five exponentials (**Supplementary Figure S2**), but only the shortest two of

these exponential components were present in the high P_o mode (**Supplementary Figure S2B**). This suggests the high P_o mode is primarily caused by suppression of the longest three apparent closed states.

The effect of NFx on the properties of single TREK-2 channels. The simple, well-behaved kinetics of TREK-2 in the high P_o mode make this gating mode ideal for analyzing the effect of channel antagonists that requires long recordings of stationary single-channel activity. We therefore focused our analysis of the effects of NFx on the single-channel gating of TREK-2 in this high P_o mode. As a control for any indirect effects of NFx on the properties of the bilayer (Kapoor et al., 2019), we first examined whether high concentrations of NFx could affect the elastic modulus of the DPhPC bilayers used in our experiments using the electrostriction method (Vitovic et al., 2013). We found no obvious effect of 1-1000 μM NFx on the modulus of elasticity ($E_\perp$, **Supplementary Figure S3**).

Recordings of a single TREK-2 channel in the high P_o mode in the presence and absence of 100μM NFx are shown in **Figure 3**. Inspection of these recordings reveals two distinct effects of the drug at all membrane voltages: a dramatic reduction in P_o along with a small reduction in the single-channel current amplitude (γ). These effects are also shown in **Figure 4A, B**.

The decrease in P_o is primarily caused by the appearance of very long closed periods that separate bursts of channel openings combined with some brief closures (**Figure 3**). Although such bursting behavior was not observed in the high P_o mode in the absence of the drug (**Figure 3**), it was consistently found in the standard (low P_o) gating mode (**Figure 2**).

The reduction in γ induced by NFx exhibited little voltage-dependence across the entire range of voltages examined (**Figure 4A**). As shown in **Figure 4B**, NFx also broadened the peak of the open current level; this effect is reminiscent of the classical open channel blocking mechanisms involving fast binding & unbinding of the blocker within the pore (Yellen, 1984).

Voltage-dependent effects of NFx on channel open probability. The inhibition of macroscopic TREK currents by NFx has previously been reported to be voltage-independent between +60 and -60 mV (Kennard et al., 2005) and when we examined its effects on P_o at the single channel level, we also found the inhibitory effect of NFx to be voltage-independent below +60 mV. However, when the P_o was measured above +60 mV, some voltage-dependence of inhibition was observed, with increased efficacy at more depolarized potentials (**Figure 4D**). Notably, the effects of voltage on the activity of these NFx-bound channels is very different from the intrinsic behavior of channels in the standard mode which exhibit strong outward rectification in the absence of NFx (**Figure 2C**); thus, NFx inhibition does not simply convert the high P_o mode to the standard mode of gating.

We therefore re-examined the voltage-dependent inhibition of macroscopic TREK-2 currents by NFx. Previous studies examined only a single, near-maximal concentration of NFx (30μM) which produces ~80% inhibition (Kennard et al., 2005). Instead, we determined macroscopic dose-response relationships for NFx inhibition at depolarized potentials (**Supplementary Figure S4**). Interestingly, this also revealed a modest voltage-dependence with a slightly increased efficacy at more positive voltages; this may account for some of the minor variations in IC_{50} values previously reported in the literature (Kennard et al., 2005; Dong et al., 2015; McClenaghan et al., 2016). It will therefore be important to take this into consideration in all future IC_{50} values reported for NFx inhibition.

The effect on NFx on TREK-2 gating kinetics. Having established its effect on single channel P_o and γ, we next examined the effect of NFx on the kinetics of channel gating. **Figure 5A** shows that in the absence of the drug, the mean open time of the single apparent open state exhibits a strong bell-shaped dependence on membrane voltage with a maximum open time around +50 mV. A previous study proposed a model of fast filter gating in K^+ channels that is primarily dependent on the electromotive force (Zilberter et al., 1988). However, this would predict a maximal open time at 0 mV in the symmetrical K^+ conditions used in our experiments and so is clearly not responsible for the fast gating we observe. **Figure 5A** also shows the dramatic decrease in mean open time caused by NFx; although the effect was sharply reduced below -50 mV and virtually absent at -100 mV (**Figure 5E**).

In the absence of NFx, the mean intrinsic short closed time (τ_F) showed an inverted bell-shaped dependence on membrane voltage with a minimum around -30 mV. Similar to the effect of NFx on the mean open time, reduction of this closed lifetime by NFx was also suppressed at negative membrane voltages (**Figure 5C,G**).

In contrast to both mean open and short closed times, the mean long closed time in the absence of the drug (τ_S) only exhibited a mild dependence on membrane voltage (**Figure 5D**). NFx reduced the mean lifetime of this component across the whole voltage range whilst its effects on the voltage dependence of the relative frequencies (areas) of the two intrinsic apparent closed states were more complex (**Figure 5B**).

Interestingly, NFx inhibition resulted in the appearance of three additional apparent closed state components (**Figure 5G,H**). These three components were present across the voltage range and their mean lifetimes were always substantially greater than the two intrinsic components present in the absence of the drug (e.g. compare **Figure 5C,D** with **Figure 6A**). Their mean lifetimes showed no obvious voltage dependence, but the relative areas (i.e. relative frequency) of the two longest states (A_4 and A_5) appeared to increase with voltage (**Figure 6B**). The steep increase in frequency of the longest closed state above +60 mV

suggests this to be the main contributing factor to the increase in NFx inhibition seen at more positive potentials (**Figure 4D**). The presence of the three long closed states is responsible for the marked decrease in channel P_o and the bursting kinetics observed in the presence of the drug (**Figure 3**). Burst analysis revealed that the three shortest closed states and two longest closed states contribute to the intraburst and interburst closings, respectively. The increase in NFx inhibition above +60 mV was accompanied by both a decrease in the mean burst length and an increase in the mean interburst close time (**Figure 6C,D**).

Taken together, this analysis of the effect of NFx on single channel behavior indicates that the drug likely exerts complex effects on all the intrinsic gating states of the channel. This is consistent with an allosteric effect in which NFx binds to all conformations of the filter gate and shifts them towards their non-conductive states.

A kinetic model for voltage-dependent gating of TREK-2 in the "high P_o" mode. Several previous studies of selectivity filter gating in related tetrameric cation channels found that voltage-dependent conformational changes can occur within the filter itself and that these changes could affect the interaction of the filter with inhibitors to alter their efficacy (Martinez-Francois et al., 2009; Posson et al., 2013). Therefore, to understand the voltage-dependent effect of NFx that we observe on channel P_O (**Figure 4D**), we first attempted to derive a kinetic scheme that can account for the intrinsic gating of TREK-2 in the high P_o mode *i.e* its properties in the absence of NFx.

The dwell time distributions were well described by three apparent states between -100 and +100 mV, but initial analysis showed that three-state kinetic models fail to adequately describe the complex voltage-dependence of channel lifetimes seen in **Figure 5**. The observed open and closed states are therefore likely to be *composites* of several states. Based on this assumption, a kinetic scheme was therefore developed that extends the number of states and which can account for this voltage-dependence (**Figure 7C**).

To model this intrinsic gating of TREK-2 in the high P_o mode, the entire voltage range between -100 and +100 mV was divided into three regions with distinct voltage dependencies for the key parameters (*i.e.* the relative areas of closed times and the mean open state (**Figure 7A,B**) and each of these regions was then considered separately. At voltages below -40mV, channel gating can be well described by a linear kinetic scheme with states O_1,C_{F1} and C_{S1} as shown in **Figure 7C**. To account for the substantial change in distribution of short and long closings and the dramatic increase in mean open time above -40 mV (**Figure 7A,B**), a second linear scheme (O_2,C_{F2} and C_{S2}) was connected to the first via their two open states (O_1 and O_2). Above +60 mV, both the mean open time and number of short closed states start to decline

with voltage and this was accounted for by adding a third linear scheme (O_3,C_{F3} and C_{S3}) and connecting O_2 with O_3.

The resulting kinetic scheme has 32 parameters and can either be fitted to the dwell-time distributions, or directly to the main distribution parameters (mean open time τ_O, mean short (τ_F) and closed (τ_S) times and their corresponding areas A_F and A_S) using the analytical expressions described in the **Supplementary Information**. We found many possible solutions when fitting this scheme to the data; one of them is depicted in detail in **Supplementary Figure S5** and the voltage-dependence of the main dwell-time distribution parameters based on this model is shown in **Figure 7D-G**.

This resulting kinetic scheme with composite states therefore represents a "core" model for TREK-2 gating at the selectivity filter in this high P_o mode. It also provides an explanation for the contrasting relationship between mean open time and P_o at high negative and positive membrane potentials (**Supplementary Figure S1**) because according to this model, the gating at these two different voltages is governed by two different open states, O_1 and O_2 (**Figure 7C**).

Modelling the effect of NFx on single-channel behavior. As described above, at potentials below -40mV, TREK-2 gating in the high P_o mode can be well described by the 3-state linear scheme (O_1, C_{F1} and C_{S1}). The simplest kinetic scheme that includes the effect of NFx bound to its two sites on the channel is a 3-state affinity allosteric model in which the three binding (k_O, k_F and k_S) and unbinding (k_{-O}, k_{-F}, k_{-S}) constants are a function of occupancy (*i.e.* the model also includes cooperativity between sites; hence the indexes 1 and 2). This model can be described as follows:

(Scheme 1)

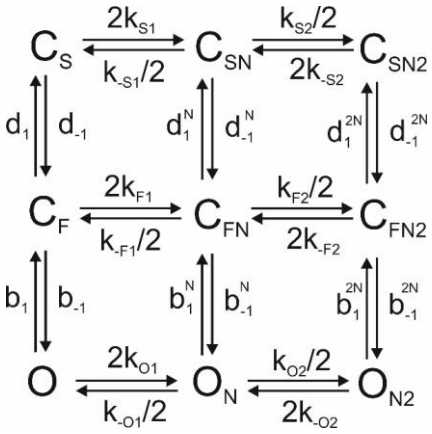

Analysis of the open and closed time distributions generated by this model showed that it cannot account for the presence of five apparent closed time components observed in the presence of NFx (**Figure 5G**). Thus, NFx does not simply alter the gating equilibrium between existing states; it either induces conformational changes that result in the creation of additional closed states and/or the full kinetic scheme of TREK-2 may contain even more kinetic states than those inferred from the voltage-dependence of gating in the absence of NFx. However, determining the precise kinetic mechanism underlying NFx inhibition would require a detailed analysis of concentration-dependent effects of NFx on gating at potentials below -40mV and this goes beyond the scope of this study. The kinetic scheme in **Figure 7C** also predicts substantial overlap of a large number of states at positive membrane potentials (**Supplementary Figure S5G**) for which precise kinetic analysis of the effects of NFx might either prove challenging or even impossible. Nevertheless, our model still provides an explanation for the increased reduction in P_o caused by NFx above +60 mV because this would arise from an increasing contribution of the states O_3, C_{F3} and C_{S3} (**Supplementary Fig S5**).

Overall, the mechanism we propose to explain this voltage-dependent inhibition builds on studies of CNG channels (Martinez-Francois et al., 2009) and of MthK where the voltage dependence of open channel block by QA ions was investigated in detail (Posson et al., 2013). This block of MthK also occurs at the selectivity filter gate and arises from voltage-dependent changes in the affinities of the open and inactivated states to these blockers (the latter occurring above +50 mV). In the case of TREK-2 in the high P_o mode, there is no obvious voltage-dependent inactivation at high voltages, but there are voltage-dependent changes in the distribution of the states which contribute to channel gating at these potentials. Unfortunately, it is not possible to obtain sufficient data to derive a similar model of gating in the standard gating mode, but both modes are still sensitive to NFx and if the mechanisms of inhibition are similar then this may also help explain the increased block of macroscopic currents we observe.

NFx does not preferentially bind to closed states of the channel. It has previously been suggested that NFx may preferentially bind to the closed states of TREK channels (Kennard et al) and this may explain why some ‘activatory’ mutations reduce the efficacy of NFx inhibition due to their increased P_O. However, if this is the case, then the NFx sensitivity of TREK-2 in the high P_O mode should be substantially lower than that observed in the standard mode. However, we found no obvious difference in the NFx sensitivity of TREK-2 channels reconstituted in lipid bilayers in these two gating modes: at 10μM, NFx blocked the high P_o and standard modes by 20 ± 0.02% (n=3; mean P_o=0.85±0.05) and 23 ± 0.05% (n=5; mean P_o=0.40±0.05); respectively. **Figure 8** shows single-channel recordings of two TREK-2

channels with two opposing extreme values of P_o (0.05 and 0.86); it is clear that the presence (or absence) of very long closed states has no obvious effect on NFx inhibition. We therefore conclude that NFx does not preferentially bind to the very long closed states; this is also consistent with our previous macroscopic studies of NFx inhibition which showed that not all activatory mutations in TREK-2 mutations necessarily reduce the NFx sensitivity of TREK-2 (McClenaghan et al., 2016).

Desensitization of NFx efficacy due to impaired channel gating. But if an increase in channel P_o does not reduce NFx efficacy then what underlies the reduced inhibition of these mutations? To address this issue, we decided to examine the effect of NFx on TREK-2 channels with the activatory Y315A mutation located within the 'hinge' of the transmembrane domains. Y315 is not part of the NFx binding site but the Y315A mutation has been reported to reduce, but not abolish, NFx inhibition (McClenaghan et al., 2016). The increased macroscopic activity of this mutation also meant that suitably long recordings of single channel inhibition by NFx were also likely to be possible and so both WT and mutant channels were heterologously expressed in HEK293 cells and their single channel behavior examined.

As expected, for wild-type TREK-2 only standard mode channels were observed with a very low P_o (ranging 0.04-0.13 at -40 mV), whereas the Y315A mutant channels exhibited markedly higher P_o (0.71 ± 0.1, n=3 at -40mV) under identical conditions. Interestingly, examination of single Y315A currents revealed a rapid 'desensitization' to NFx inhibition. **Figure 9A** shows that the P_o was initially reduced >90% by 10 μM NFx (for comparison, the P_o of WT TREK-2 channel was reduced by 79 ± 0.05% n=6). However, within ~30 seconds, this inhibitory effect was dramatically reduced.

Similar to its effect on WT TREK-2, NFx also reduced the single-channel current amplitude of Y315A TREK-2 and this effect was not abolished by desensitization (**Figure 8B**). Subsequent application of 100 μM NFx further decreased channel P_O but this effect also reversed within ~1 minute so that the channel P_o before and after addition of 100 μM NFx were practically identical (**Figure 9A**). In addition to its relatively transient effect on channel P_o, 100 μM NFx also reduced γ even further, but this was partially reversed by desensitization (**Figure 9C**). Interestingly, channel desensitization in the presence of 100 μM NFx was accompanied by the appearance of two distinct subconductance levels - one above main open and one above closed current level (**Figure 9C**).

The desensitization of TREK-2 to NFx might arise from several possible mechanisms. It could be caused by (i) abolished drug binding to the channel, (ii) a suppressed ability of the bound drug to directly impair ionic flux through the channel (if we assume that NFx bound under the selectivity filter directly affects flow of K^+ via electrostatic repulsion or physical occlusion), or

(iii) suppresses the ability of the bound drug to allosterically inhibit the channel via the filter gate itself.

The observation that NFx can still reduce γ even when its effect on P_o is virtually abolished by desensitization (**Figure 9C**) indicates the drug still remains bound to the channel in this desensitized state, and that its effect on selectivity filter gating must be impaired instead. Interestingly, the appearance of substates due to desensitization indicates that that this process may also destabilize the 'normal' open and closed conformations of the selectivity filter. Together, these results therefore indicate that the reduced NFx sensitivity of this mutation is primarily due to impaired transduction between the binding and gating events involved in inhibition, and is not a simple consequence of an increased P_O.

Electrostatic effects of NFx binding do not contribute to inhibition. At physiological pH, NFx is normally positively charged and **Figure 1A** shows that it binds within the fenestrations of TREK-2 where its charged -NH_3^+ group faces the permeation pathway. We therefore decided to examine whether this positive charge may affect K^+ permeation and thereby contribute to the effects of NFx on P_o and/or γ.

To first explore this we used the crystal structure of TREK-2 obtained with NFx bound (4XDK) and performed Poisson-Boltzmann electrostatic calculations for K^+ moving along the axis of the pore in either the presence or absence of NFx. These calculations revealed only a modest increase in barrier to K^+ permeation contributed by the presence of charged NFx (**Figure 10A**). To further explore this, we next tested the effect of desamino chloro-fluoxetine, a 'neutralized' derivative of NFx where the positively charged -NH_3^+ group is substituted by chlorine. As shown in **Figure 10B, C**, when 10μM desamino chloro-fluoxetine was tested on the activity of wild-type TREK-2 channels expressed in HEK293 cells it also markedly reduced channel P_o (75 ± 0.05%; n=5) with a concomitant reduction in γ. (15 ± 5%; n=5) and was similar to that produced by NFx under identical conditions (70 ± 0.03% for P_o and 11 ± 7% for γ, respectively n=5). Together these results suggest that the charged nature of NFx contributes little to its inhibitory effects on channel activity.

ML335 activated state of the filter gate antagonizes NFx inhibition. We have shown above that activation by ML335 dramatically antagonizes the inhibitory effect of NFx on macroscopic TREK-2 currents (**Figure 1**). We therefore examined this antagonistic effect at the single-channel level on WT TREK-2 expressed in HEK293 cells. Interestingly, we observed that 100 μM ML335 caused either partial or full activation of single TREK-2 channels (**Supplementary Figure 6**), an effect similar to that of many known ion channel agonists. However, the mean P_o in the presence of 100 μM ML335 was 0.69±0.2 (n=4) and regardless of whether activation by ML335 was partial or maximal, any subsequent application of 10 μM NFx failed to elicit any

visible effects on channel gating: the mean P_o in the presence of both 100 μM ML335 and 10μM NFx was 0.69±0.2 (n=4). Furthermore, ML335 activation also completely abolished the effects of NFx on single channel current amplitude as the amplitude ratio of γ in both conditions was identical (1.00 ± 0.01, n=4) (**Supplementary Figure 6**).

From the position of the known binding sites of both drugs within the channel (**Figure 1A, B**) it is clear that ML335 is unlikely to directly compete with the binding of NFx. Instead the reduced efficacy of NFx may be due to the fact that ML335 activation of the filter gate interferes with the transduction mechanism involved in NFx inhibition of the filter gate. However, ML335 might also indirectly affect the ability of NFx to bind to the channel. The fact that application of NFx does not reduce γ in ML335-activated channels is consistent with the idea that NFx cannot bind, and it is interesting to note that many different structures of TREK1 have been cocrystallised with ML335 and they all appear in the up state which lacks a binding site for NFx (Lolicato et al., 2017; Lolicato et al., 2020). Either way, the fact that ML335 impairs the effect of NFx on P_o and γ implies both these effects are mediated via allosteric mechanisms which converge on the filter gate. Overall, the different effects of these various agonists on NFx inhibition demonstrates the filter gate can be activated by structurally distinct mechanisms that likely reflect the polymodal regulation of this channel. It will therefore be interesting to understand why binding of this specific agonist so profoundly disrupts the action of NFx.

Conclusions

In summary, our results provide a more detailed description for the behavior of TREK-2 at the single channel level and provide insight into the mechanism of TREK-2 inhibition by NFx as well as its activation by ML335. The effects of NFx on TREK-2 activity are complex and involve both a reduction in single channel open probability and single channel conductance. Our results indicate that these two effects are mediated via distinct mechanisms, both involving allosteric modulation of the selectivity filter. We also uncovered a voltage-dependent effect of NFx on channel P_o at more depolarized potentials that may result from different open and closed conformations adopted by the selectivity filter gate at different membrane potentials. These studies of TREK-2 inhibition at the single channel level now complement the wealth of structural information available for this channel and increase our understanding of the complex ways in which these different drugs can modulate K2P channel activity.

Materials and Methods

Preparation of TREK-2 containing Giant Unilamellar Vesicles. Human TREK-2 (*KCNK10*) 'crystal construct' protein (Gly67 to Glu340) was expressed and purified as previously described (Dong et al) with the exception that it was purified in 1% w/v n-Octyl-β-D-Glucoside, 0.1% w/v cholesteryl hemisuccinate. 1,2-diphytanoyl-sn-glycero-3-phosphocholine (DPhPC) was dissolved in chloroform to a concentration of 10 mM and stored at -20°C. The GUVs where then made by electroformation in a 1 M sorbitol solution using the Vesicle Prep Pro (Nanion Technologies, GmbH). Purified TREK-2 was then mixed with GUVs to a final concentration of ~1 - 5 µg/ml and incubated overnight at 4 °C with 0.5mg/ml Bio-Beads (Bio-Rad) prior to use.

Clones and Chemicals. Full length human TREK-2 isoform 3 (NP_612191) was used throughout this study and was subcloned into the pFAW vector for expression in oocytes. The truncated construct used to generate protein (TREK-2ΔN/ΔC) is identical to that used previously to obtain crystal structures (Dong et al., 2015); it contains a deletion of 71 residues at the N-terminus and 213 residues at the C-terminus. NFx and desamino chloro-fluoxetine (Toronto Research Chemicals). NFx was dissolved in DMSO and diluted to working concentrations on the day of experimenting (max final DMSO concentration was 0.3 %). Desamino chloro-fluoxetine was dissolved in chloroform and diluted to working concentrations on the day of experimenting (max final concentration was 0.01 %).

Bilayer recordings and analysis. All electrophysiological recordings were performed with the Nanion Port-a-Patch system connected to an Axopatch 200B amplifier via a Digidata 1440A digitizer (Molecular Devices). Data was filtered at 5 kHz and recorded at a 200 kHz sampling rate with program Clampex (Molecular Devices). Experiments were carried out in symmetrical 200 mM KCl, 10 mM HEPES (pH 6.0 with KOH) solutions. Single-channel currents were idealized using 50% threshold criterion with program Clampfit (Molecular Devices) at an imposed resolution of 50µs. Only one open and one closed level was considered in the analysis – all subconductance states were neglected (these typically comprised less than 1% of open and closed level events of channels in the "high P_O" mode. Analysis of amplitude and dwell-time distributions was carried out in Origin (OriginLab Corporation) and an in-house software written in Mathematica (Wolfram Technologies). Empirical correction for open times due to missed events was carried out as described previously by (Davies et al., 1992). Critical time for burst analysis was determined using Colquhoun and Sakmann criterion (Colquhoun et al., 1992)

Electrostriction measurements. Membrane elasticity measurements were performed as described previously (Vitovic et al., 2013). Briefly, 1kHz sinewave with an amplitude of 100mV

was applied to the membrane using a wave generator (Rigol DG821, Rigol technologies). Due to the non-linear dependence of membrane capacitance on the voltage V ($C = C_0 (1 + \alpha V^2)$, where C_0 is the capacitance at V = 0 and α is the electrostriction coefficient), third current harmonic with frequency 3 kHz and amplitude A_3 is generated in addition to the basic first current harmonic, A_1 (frequency 1 kHz). The ratio of modulus of elasticity with and without NFx ($E_{\perp NFX}/E_{\perp}$ (0)) is then given as $A_3(0)/A_{3NFX}$, where $A_3(0)$ and A_{3NFX} are amplitudes of third current harmonic frequencies in the absence and presence of NFx, respectively.

Expression in Oocytes and HEK293 Cells Oocytes were prepared for injection of mRNA by collagenase digestion followed by manual defolliculation and stored in ND96 solution which contained (in mM): 96 NaCl, 2 KCl, 1.8 $CaCl_2$, 1 $MgCl_2$, 10 HEPES, (pH 7.4) and was supplemented with 2.5 mM sodium pyruvate 50 µg/ml gentamycin, 50 µg/ml tetracycline, 50µg/ml ciprofloxacin and 100 µg/ml amikacin. Cells were injected with 1-4 ng of mRNA up to 4 days post isolation. In vitro transcription of mRNA was done using the Amplicap™ SP6 Kit, (Cambio). Experiments were performed 12-24 hours post injection at room temperature (22 °C unless otherwise indicated). For measurement and comparison of basal whole-cell currents oocytes were injected with 4 ng of RNA and recorded exactly 24 hours post injection.

HEK293 cells were cultured in DMEM (Sigma) containing 10% FBS (Life Technologies), 3 mM glucose, and 2 mM glutamine at 37°C in a humidified atmosphere of 5% CO_2/95% O_2 at 37°C. Cells were transiently transfected with 0.2 μg of channel pcDNA3 per dish using FuGENE 6 according to the manufacturers' instructions. Cells were used 1–2 days after transfection.

Electrophysiology in heterologous systems and data analysis. For currents recorded in *Xenopus* oocytes: Giant-patch electrodes were pulled from thick-walled borosilicate glass and polished to give pipette resistances around 0.3-0.5 MΩ when filled with patch solution. Pipette solution contained (in mM) 116 NMDG, 4 KCl, 1 $MgCl_2$, 3.6 $CaCl_2$, 10 HEPES (pH 7.4); whilst bath solution contained (in mM) 120 KCl, 1 NaCl, 2 EGTA, 10 HEPES (pH 7.3). Patches were perfused via a gravity flow perfusion system. a HEKA EPC 10 USB single computer controlled amplifier and recorded using a Patchmaster v2x90.5 (HEKA electronics), filtered at 1 kHz and sampled at 10 kHz. For currents recorded in HEK293 cells*:* Patch electrodes were pulled from thick-walled borosilicate glass and polished to give pipette resistances around 3-5 MΩ when filled with patch solution. The currents were recorded from excised patches with both intracellular and extracellular solution containing 200 mM KCl, 10 mM HEPES (pH 6.0 with KOH). Patches were perfused via a gravity flow perfusion system. Data was acquired with pClamp and recorded using an Axopatch 200B (Molecular Devices), filtered at 5 kHz and sampled at 200 kHz. Single channel currents were analyzed in an identical manner to those obtained from bilayers (see above).

The macroscopic concentration-inhibition relationships in Figure 1 were fitted with a modified Hill equation:

$$\frac{I}{I_0} = a + \frac{1-a}{1+(\frac{[X]}{IC_{50}})^h} \qquad \text{(eq 1)}$$

Where *I* and I_O is the current in the presence and absence of inhibitor, *[X]* is the concentration of inhibitor, IC_{50} is the inhibitor concentration at which the inhibition is half maximal, *h* is the Hill coefficient and *a* is the fraction of unblockable current; *a*=0 except where indicated in legend to Figure 1.

The macroscopic concentration-activation relationships in Figure 1E were fitted with a modified Hill equation:

$$\frac{I}{I_0} = a + \frac{(1-a)(\frac{[X]}{IC_{50}})^h}{1+(\frac{[X]}{IC_{50}})^h} \qquad \text{(eq 2)}$$

Where *I* and I_O is the current in the presence and absence of agonist, *[X]* is the concentration of agonist, IC_{50} is the agonist concentration at which the activation is half maximal, *h* is the Hill coefficient and *a* is the fraction of initial current.

Poisson-Boltzmann electrostatics. Born energy profiles of a K^+ ion through the channel pore of a TREK-2 structure (PDB ID: 4XDK) in the absence or presence of NFx, were calculated by numerically solving the linearized Poisson-Boltzmann equation using the Adaptive Poisson-Boltzmann Solver (Baker et al., 2001; Jurrus et al., 2018). The ion was positioned along the central channel axis at 0.05 nm intervals, extending 2 nm into the bulk phase from either side of the channel. A Born radius of 0.22 nm was used for K^+. Protein and ligand atoms were assigned radii and partial charges from the CHARMM36 force field. The radius of an implicit solvent molecule was set to 0.14 nm, the ionic strength to 0.15 M KCl, and the dielectric constant to 78.5 for the solvent and 2 for the protein. The Born energy for inserting an ion at each sampled position was calculated at 37 °C by subtracting the individual electrostatic energies of the protein and the ion in solution from the electrostatic energy of the protein-ion system (Beckstein et al., 2004).

Acknowledgements

We thank members of our labs for helpful comments on the manuscript and Mark Sansom for his support of the project. This work was supported by the BBSRC, the Wellcome Truts and by the Deutsche Forschungsgemeinschaft (DFG) as part of the Research Unit FOR2518, DynIon.

The authors declare no financial interests.

Figure Legends

Figure 1: Direct and allosteric interactions of NFx with TREK-2.

A. Structure of TREK-2 in the down state showing norfluoxetine (NFx) bound within the fenestrations (PDB ID: 4XDK). **B.** Schematic drawing of TREK-2 with relative position of various bound agonists and antagonists. QA+ represents either TEA, TPA or THexA. **C.** Representative traces of macroscopic TREK-2 currents elicited by voltage ramps between -80 and +80mV in giant excised patches from *Xenopus* oocytes measured in control solution and various bath concentrations of NFx, as indicated. **D**. Similar representative traces of macroscopic TREK-2 currents showing reduced inhibition by NFx in the presence of 80 μM TPA. Block by 80 μM TPA alone shown in red. **E.** NFx inhibition of TREK-2 currents at +40 mV in *Xenopus* oocytes on its own (IC_{50}=2.7 μM; *h*=1.0 n=19) and in the presence of 100 mM TEA (IC_{50}=3.8 μM; *h*=0.8 n=7) or 80μM TPA (IC_{50}=65μM; *h*=1.2 *a*=0.05; n=12), as indicated. **F.** BL1249 activation of TREK-2 currents in *Xenopus* oocytes on its own (IC_{50}=2.5μM; *h*=1.9, n=13) and in the presence of 5μM THexA (IC_{50}=25μM; *h*=2.2, n=13) or 5μM NFx (IC_{50}=9.9μM; *h*=1.8; n=17), as indicated. **G**. Representative traces of macroscopic TREK-2 currents elicited by voltage ramps between -80 and +80mV in giant excised patches from *Xenopus* oocytes measured in control solution, in the presence of 50μM ML-335 alone and with added various bath concentrations of NFx, as indicated. **H**. NFx inhibition of TREK-2 currents in *Xenopus* oocytes on its own (IC_{50}=2.7μM; *h*=1.7 n=19) and in the presence of 1mM 2-APB (IC_{50}=3.8μM; *h*=0.6 n=11) or 50μM ML-335 (IC_{50}=164μM; *h*=0.8; n=7), as indicated.

Figure 2: Two types of TREK-2 behavior in lipid bilayers.

A,B. Single-channel recordings of TREK-2 incorporated into a bilayer at +80mV (top trace) and -80mV (bottom trace). The dotted line represents the closed channel level. **C,D.** Macroscopic current -voltage relationships simulated for one hundred TREK-2 channels using values of single-channel open probability (P_O) and single-channel current amplitude (*i*) obtained from single-channel recordings of TREK-2 with standard (**C**) and "high P_O" behavior (**D**). The lines are fit by hand.

Figure 3. Effect of 100μM NFx on a single TREK-2 channel. Single-channel recordings of TREK-2 in in the high P_o gating mode at different membrane voltages between +100mV and -100mV in the absence (left) and presence (right) of 100μM NFx. Dotted lines represent the closed channel levels.

Figure 4. Summary of the effects of NFx on TREK-2 single channels.

A. The mean single-channel conductance of TREK-2 in the absence (open circles; n=3) and presence of 100μM NFx (filled circles; n=3). **B.** Histograms of open single-channel current level in the absence (black line) and presence (grey line) of 100μM NFx at +100mV (top) and -100mV (bottom). **C.** Mean single-channel open probability of TREK-2 in the absence (open circles; n=3) and presence of 100μM NFx (filled circles; n=3). **D.** Mean single-channel current conductance (filled squares) and mean single-channel open probability (filled circles) in the presence of 100μM NFx normalized to values obtained in the absence of NFx (n=3).

Figure 5. Effect of NFx on single-channel kinetics

A. Mean open time as a function of membrane voltage in the absence (open circles) and presence of 100μM NFx (filled circles) in single-channel recordings depicted in Figure 4. The lines through the data are drawn by hand. **B.** Relative areas of the shortest (squares) and the second shortest (circles) closed states in the absence (open symbols) and presence (filled symbols) of 100μM NFx. **C.** Mean shortest closed time as a function of membrane voltage in the absence (open circles) and presence of 100μM NFx (filled circles). **D.** Mean second shortest closed time as a function of membrane voltage in the absence (open circles) and presence of 100μM NFx (filled circles). **E.** Distribution of open times in the absence (open bars) and presence (filled bars) of 100μM NFx at -100mV. **F.** Distribution of open times in the absence (open bars) and presence (filled bars) of 100μM NFx at +100mV. **G.** Distribution of closed times in the absence (open bars) and presence (filled bars) of 100μM NFx at -100mV. **H.** Distribution of closed times in the absence (open bars) and presence (filled bars) of 100μM NFx at +100mV.

Figure 6. Properties of long closed states and bursts in the presence of NFx

Mean lifetimes (**A**) and relative areas (**B**) of three apparent long closed states observed in the presence of 100μM NFx in single channel recordings depicted in Figure 4. The lines through the data are fit by hand. **C,D.** The dependence of the mean burst duration and the mean inter-burst closure on the membrane voltage in the presence of 100μM NFx. The lines are fit by hand.

Figure 7. Kinetic model of gating at the selectivity filter.

A. Voltage-dependence of relative areas of fast and long closed states. Three distinct regions characterized by different voltage-dependence are depicted in different shades of grey. **B.** Voltage-dependence of mean open times. Three distinct regions of behavior at these different voltages are highlighted in shades of grey. The dotted line represents values predicted by the

left arm of the kinetic model shown in panel C (including states O_1, C_{F1},C_{S1}). **C.** A kinetic scheme of the TREK-2 selectivity filter gate with three sets of open (O), short (C_F) and long closed states (C_S) affecting three distinct voltage regions depicted in panels A & B.
E-H. Voltage-dependence of intrinsic mean open time **(E)**, short closed time **(F)**, long closed time **(G)** and relative areas of short and long closed times **(H)**. The lines are a fit of the kinetic model in Panel **C** to the data shown in Figure 5.

Figure 8. Relative P_o does not define the efficacy of NFx inhibition.
Single-channel recordings at +60mV of a single TREK-2 channel reconstituted in a bilayer with low (top two trace) and high P_o (bottom two traces) in the absence and presence of 10μM NFx as indicated. Dotted line represents the closed channel level. The relative change in P_o is similar in both cases.

Figure 9. Desensitization of NFx Effects on TREK-2 Y315A.
A. Single-channel recordings of TREK-2 Y315A mutant channels recorded at +40mV in excised patches from HEK293 cells in the presence and absence of either 10μM or 100μM NFx before and after channel desensitization. **B,C.** Histograms of single channel current amplitudes obtained in control solution and in the presence of 10μM or 100μM NFx before and after desensitization as indicated. For clarity, all amplitude histograms were scaled to the same open channel level.

Figure 10. Effect of Desamino chloro-fluoxetine on TREK-2 channels.
A. Electrostatic profile of a K^+ through the pore of the TREK-2 channel in the presence and absence of NFx. The relevant region where NFx binds just below the filter is expanded below and shows two independent calculations in the presence of NFx compared to the Apo structure. A minor increase in the barrier for K^+ permeation is seen in the presence of two charged NFx molecules bound at their sites below the filter. **B.** Single-channel recording of TREK-2 channel at -40mV in an excised patch from HEK293 cells either in the absence or presence of 10μM desamino chloro-fluoxetine as indicated. Dotted lines in top traces represent the closed channel level. **C.** Histograms of single channel currents from recordings shown above. For clarity, both amplitude histograms were scaled to the same open channel level. The chemical structure of desamino chloro-fluoxetine is shown on the left.

References

Armstrong CM. 1971. Interaction of tetraethylammonium ion derivatives with the potassium channels of giant axons. *J Gen Physiol*. 58:413-437.

Aryal P, Jarerattanachat V, Clausen MV, Schewe M, McClenaghan C, Argent L, Conrad LJ, Dong YY, Pike ACW, Carpenter EP *et al.* 2017. Bilayer-Mediated Structural Transitions Control Mechanosensitivity of the TREK-2 K2P Channel. *Structure*. 25:708-718 e702.

Bagriantsev SN, Peyronnet R, Clark KA, Honore E, and Minor DL, Jr. 2011. Multiple modalities converge on a common gate to control K2P channel function. *EMBO J*. 30:3594-3606.

Baker NA, Sept D, Joseph S, Holst MJ, and McCammon JA. 2001. Electrostatics of nanosystems: application to microtubules and the ribosome. *Proc Natl Acad Sci U S A*. 98:10037-10041.

Baukrowitz T, and Yellen G. 1996. Use-dependent blockers and exit rate of the last ion from the multi-ion pore of a K+ channel. *Science*. 271:653-656.

Beckstein O, Tai K, and Sansom MS. 2004. Not ions alone: barriers to ion permeation in nanopores and channels. *J Am Chem Soc*. 126:14694-14695.

Clausen MV, Jarerattanachat V, Carpenter EP, Sansom MSP, and Tucker SJ. 2017. Asymmetric mechanosensitivity in a eukaryotic ion channel. *Proc Natl Acad Sci U S A*. 114:E8343-E8351.

Colquhoun D, Jonas P, and Sakmann B. 1992. Action of brief pulses of glutamate on AMPA/kainate receptors in patches from different neurones of rat hippocampal slices. *J Physiol*. 458:261-287.

Davies NW, Standen NB, and Stanfield PR. 1992. The effect of intracellular pH on ATP-dependent potassium channels of frog skeletal muscle. *J Physiol*. 445:549-568.

Djillani A, Mazella J, Heurteaux C, and Borsotto M. 2019a. Role of TREK-1 in Health and Disease, Focus on the Central Nervous System. *Front Pharmacol*. 10:379.

Djillani A, Pietri M, Mazella J, Heurteaux C, and Borsotto M. 2019b. Fighting against depression with TREK-1 blockers: Past and future. A focus on spadin. *Pharmacol Ther*. 194:185-198.

Dong YY, Pike AC, Mackenzie A, McClenaghan C, Aryal P, Dong L, Quigley A, Grieben M, Goubin S, Mukhopadhyay S *et al.* 2015. K2P channel gating mechanisms revealed by structures of TREK-2 and a complex with Prozac. *Science*. 347:1256-1259.

Enyedi P, and Czirjak G. 2010. Molecular background of leak K+ currents: two-pore domain potassium channels. *Physiol Rev*. 90:559-605.

Heurteaux C, Lucas G, Guy N, El Yacoubi M, Thummler S, Peng XD, Noble F, Blondeau N, Widmann C, Borsotto M *et al.* 2006. Deletion of the background potassium channel TREK-1 results in a depression-resistant phenotype. *Nat Neurosci*. 9:1134-1141.

Jurrus E, Engel D, Star K, Monson K, Brandi J, Felberg LE, Brookes DH, Wilson L, Chen J, Liles K *et al.* 2018. Improvements to the APBS biomolecular solvation software suite. *Protein Sci*. 27:112-128.

Kang D, Choe C, Cavanaugh E, and Kim D. 2007. Properties of single two-pore domain TREK-2 channels expressed in mammalian cells. *J Physiol*. 583:57-69.

Kapoor R, Peyear TA, Koeppe RE, 2nd, and Andersen OS. 2019. Antidepressants are modifiers of lipid bilayer properties. *J Gen Physiol*. 151:342-356.

Kennard LE, Chumbley JR, Ranatunga KM, Armstrong SJ, Veale EL, and Mathie A. 2005. Inhibition of the human two-pore domain potassium channel, TREK-1, by fluoxetine and its metabolite norfluoxetine. *Br J Pharmacol*. 144:821-829.

Lolicato M, Arrigoni C, Mori T, Sekioka Y, Bryant C, Clark KA, and Minor DL, Jr. 2017. K2P2.1 (TREK-1)-activator complexes reveal a cryptic selectivity filter binding site. *Nature*. 547:364-368.

Lolicato M, Natale AM, Abderemane-Ali F, Crottès D, Capponi S, Duman R, Wagner A, Rosenberg JM, Grabe M, and Minor DL. 2020. K_{2P} channel C-type gating involves asymmetric selectivity filter order-disorder transitions. *bioRxiv*.2020.2003.2020.000893.

Martinez-Francois JR, Xu Y, and Lu Z. 2009. Mutations reveal voltage gating of CNGA1 channels in saturating cGMP. *J Gen Physiol*. 134:151-164.

Mathie A, and Veale EL. 2015. Two-pore domain potassium channels: potential therapeutic targets for the treatment of pain. *Pflugers Arch*. 467:931-943.

McClenaghan C, Schewe M, Aryal P, Carpenter EP, Baukrowitz T, and Tucker SJ. 2016. Polymodal activation of the TREK-2 K2P channel produces structurally distinct open states. *J Gen Physiol*. 147:497-505.

Niemeyer MI, Cid LP, Gonzalez W, and Sepulveda FV. 2016. Gating, Regulation, and Structure in K2P K+ Channels: In Varietate Concordia? *Mol Pharmacol*. 90:309-317.

Piechotta PL, Rapedius M, Stansfeld PJ, Bollepalli MK, Ehrlich G, Andres-Enguix I, Fritzenschaft H, Decher N, Sansom MS, Tucker SJ *et al.* 2011. The pore structure and gating mechanism of K2P channels. *EMBO J*. 30:3607-3619.

Posson DJ, McCoy JG, and Nimigean CM. 2013. The voltage-dependent gate in MthK potassium channels is located at the selectivity filter. *Nat Struct Mol Biol*. 20:159-166.

Rapedius M, Schmidt MR, Sharma C, Stansfeld PJ, Sansom MS, Baukrowitz T, and Tucker SJ. 2012. State-independent intracellular access of quaternary ammonium blockers to the pore of TREK-1. *Channels (Austin)*. 6:473-478.

Rodstrom KEJ, Kiper AK, Zhang W, Rinne S, Pike ACW, Goldstein M, Conrad LJ, Delbeck M, Hahn MG, Meier H *et al.* 2020. A lower X-gate in TASK channels traps inhibitors within the vestibule. *Nature*. 582:443-447.

Schewe M, Nematian-Ardestani E, Sun H, Musinszki M, Cordeiro S, Bucci G, de Groot BL, Tucker SJ, Rapedius M, and Baukrowitz T. 2016. A Non-canonical Voltage-Sensing Mechanism Controls Gating in K2P K+ Channels. *Cell*. 164:937-949.

Schewe M, Sun H, Mert U, Mackenzie A, Pike ACW, Schulz F, Constantin C, Vowinkel KS, Conrad LJ, Kiper AK *et al.* 2019. A pharmacological master key mechanism that unlocks the selectivity filter gate in K(+) channels. *Science*. 363:875-880.

Simkin D, Cavanaugh EJ, and Kim D. 2008. Control of the single channel conductance of K2P10.1 (TREK-2) by the amino-terminus: role of alternative translation initiation. *J Physiol*. 586:5651-5663.

Vitovic P, Subjakova V, and Hianik T. 2013. The physical properties of lipid monolayers and bilayers containing calixarenes sensitive to cytochrome c. *Gen Physiol Biophys*. 32:189-200.

Vivier D, Bennis K, Lesage F, and Ducki S. 2016. Perspectives on the Two-Pore Domain Potassium Channel TREK-1 (TWIK-Related K(+) Channel 1). A Novel Therapeutic Target? *J Med Chem*. 59:5149-5157.

Yellen G. 1984. Ionic permeation and blockade in Ca2+-activated K+ channels of bovine chromaffin cells. *J Gen Physiol*. 84:157-186.

Zhuo RG, Liu XY, Zhang SZ, Wei XL, Zheng JQ, Xu JP, and Ma XY. 2015. Insights into the stimulatory mechanism of 2-aminoethoxydiphenyl borate on TREK-2 potassium channel. *Neuroscience*. 300:85-93.

Zilberter Y, Burnashev N, Papin A, Portnov V, and Khodorov B. 1988. Gating kinetics of ATP-sensitive single potassium channels in myocardial cells depends on electromotive force. *Pflugers Arch*. 411:584-589.

Figure 1

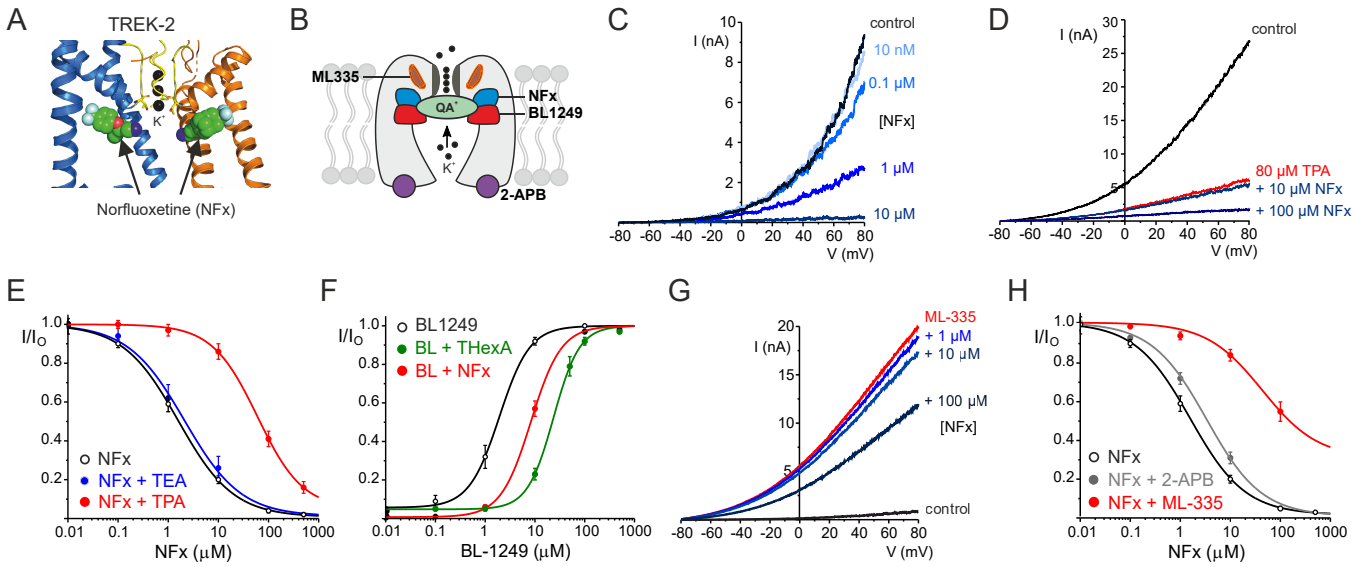

Figure 2

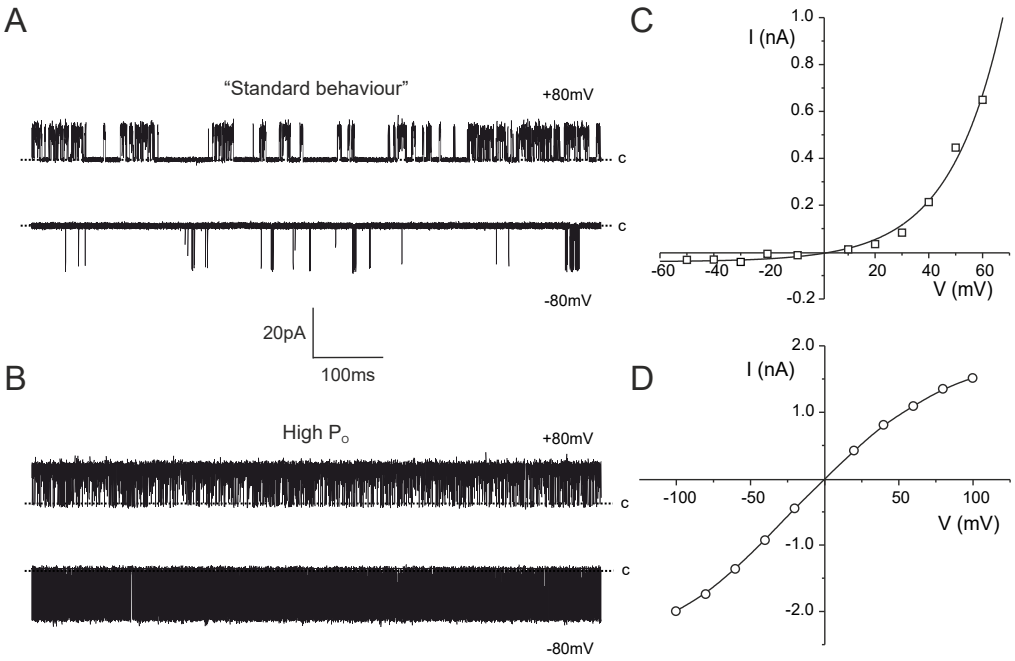

Figure 3

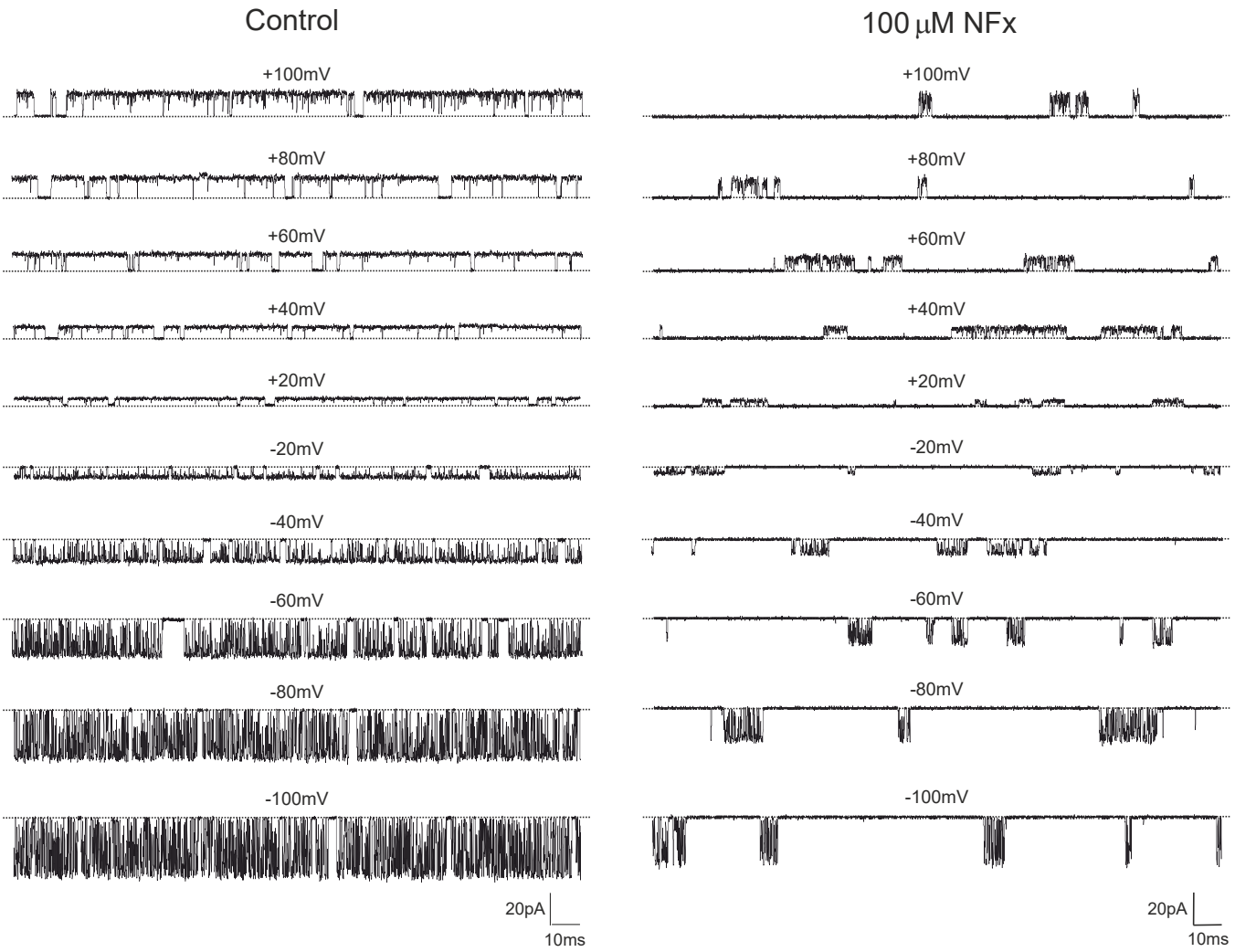

Figure 4

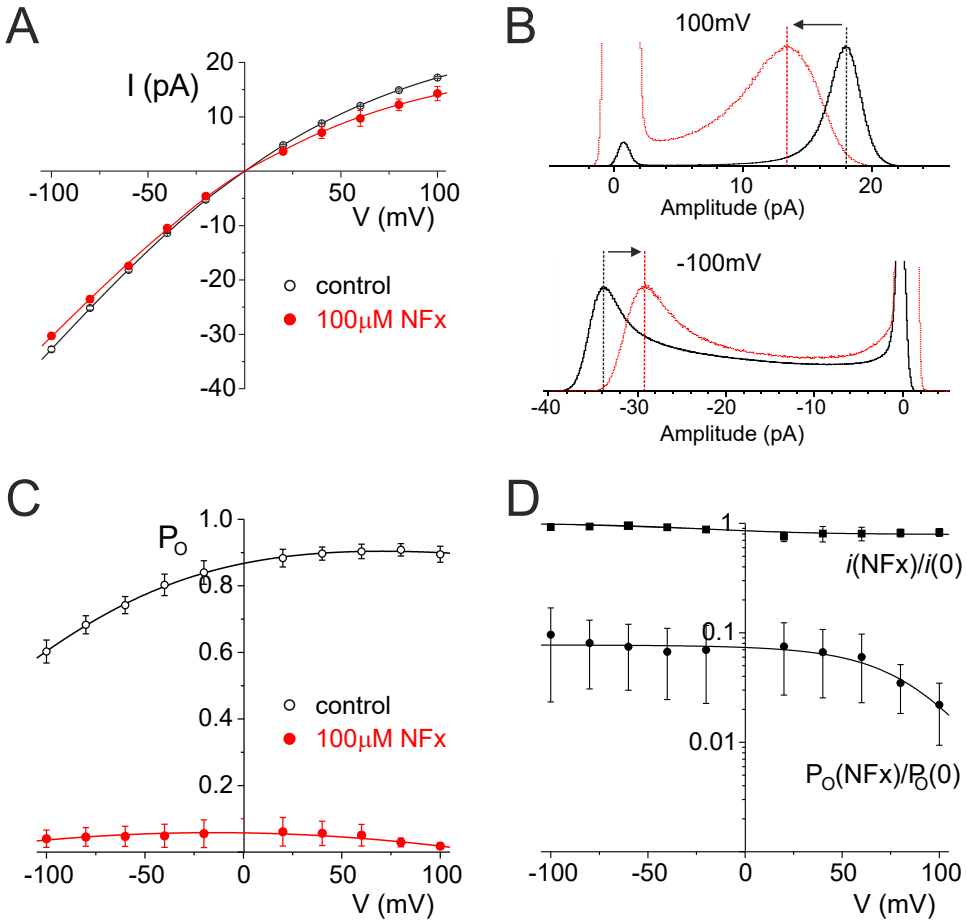

Figure 5

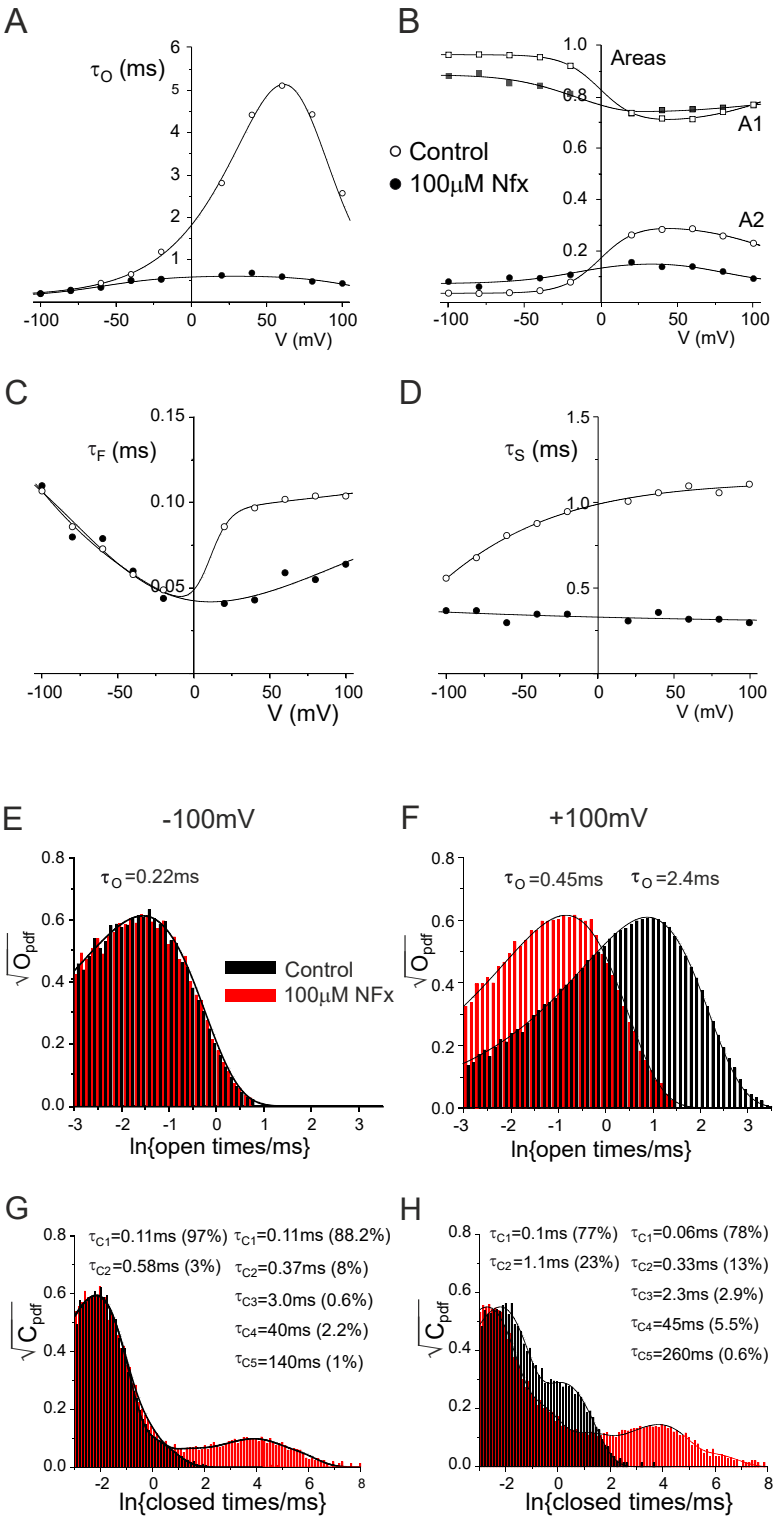

Figure 6

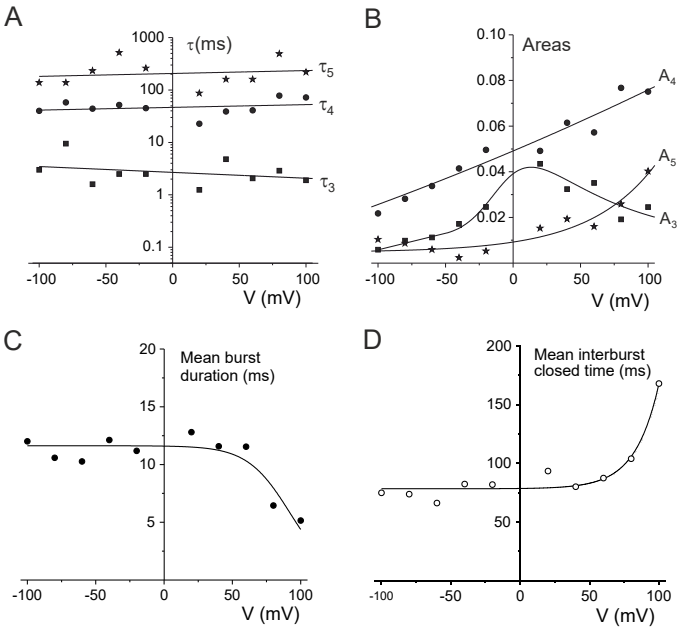

Figure 7

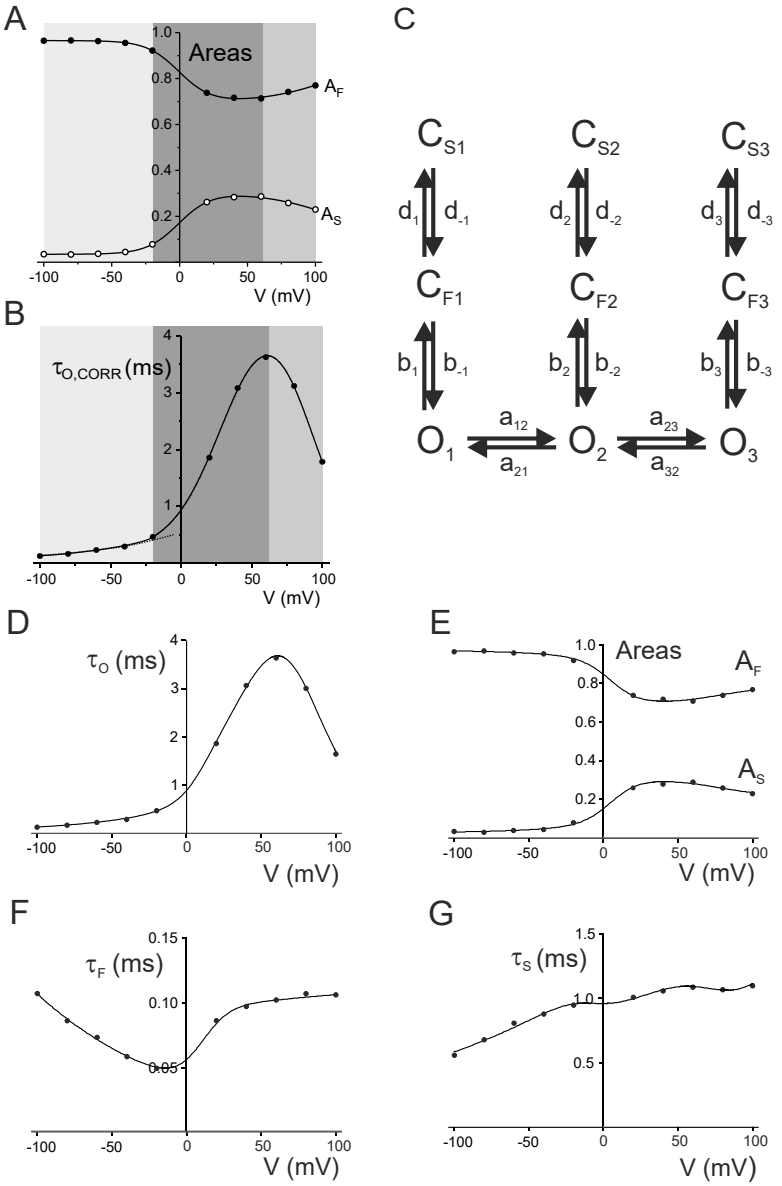

Figure 8

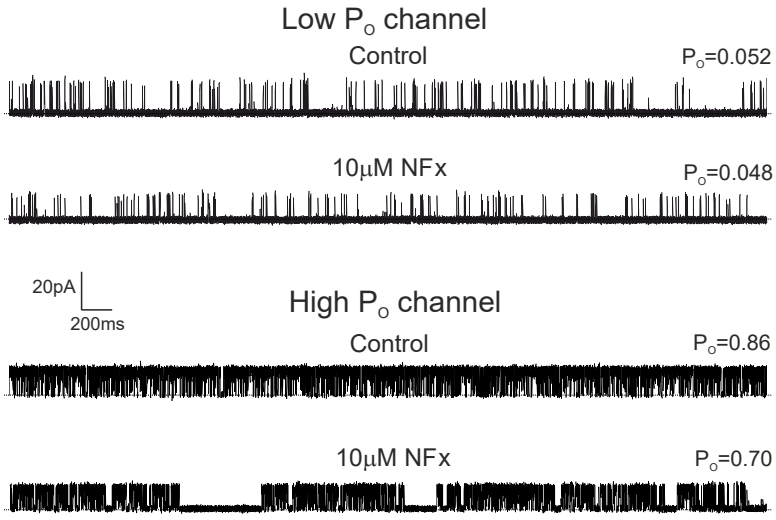

Figure 9

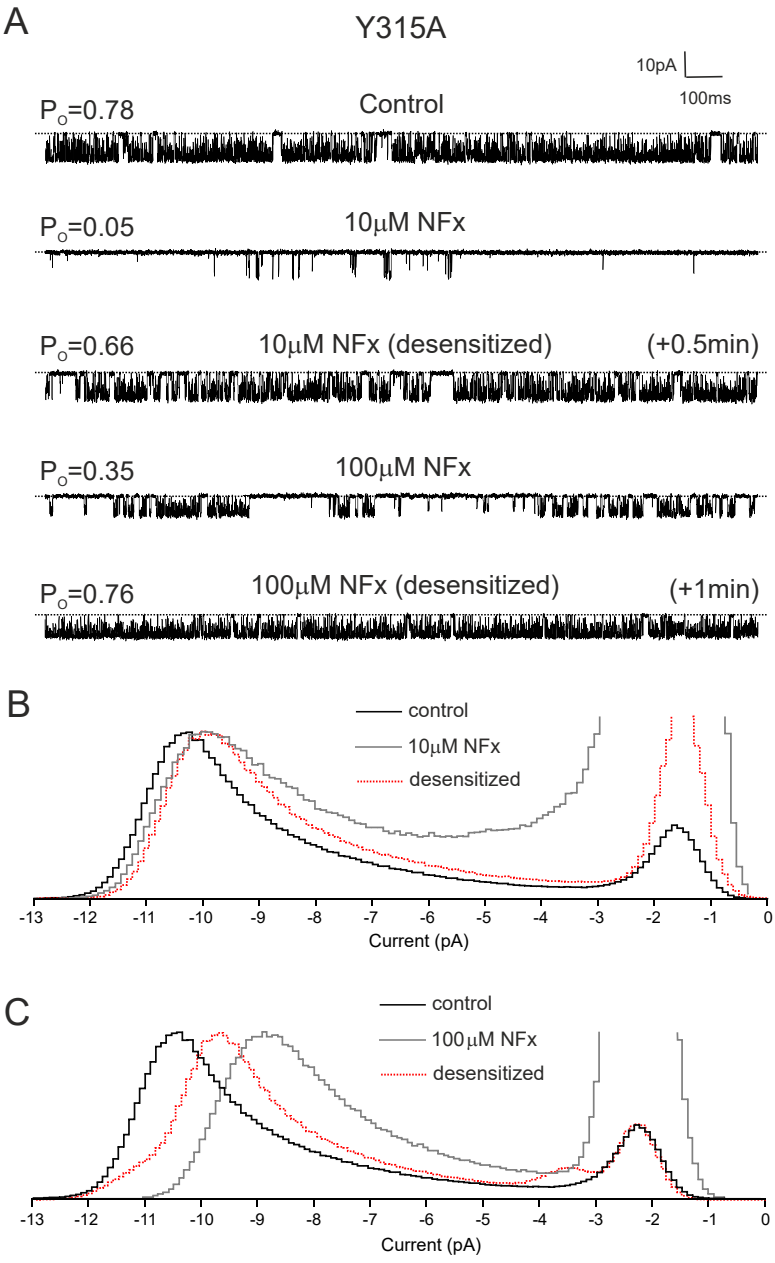

Figure 10

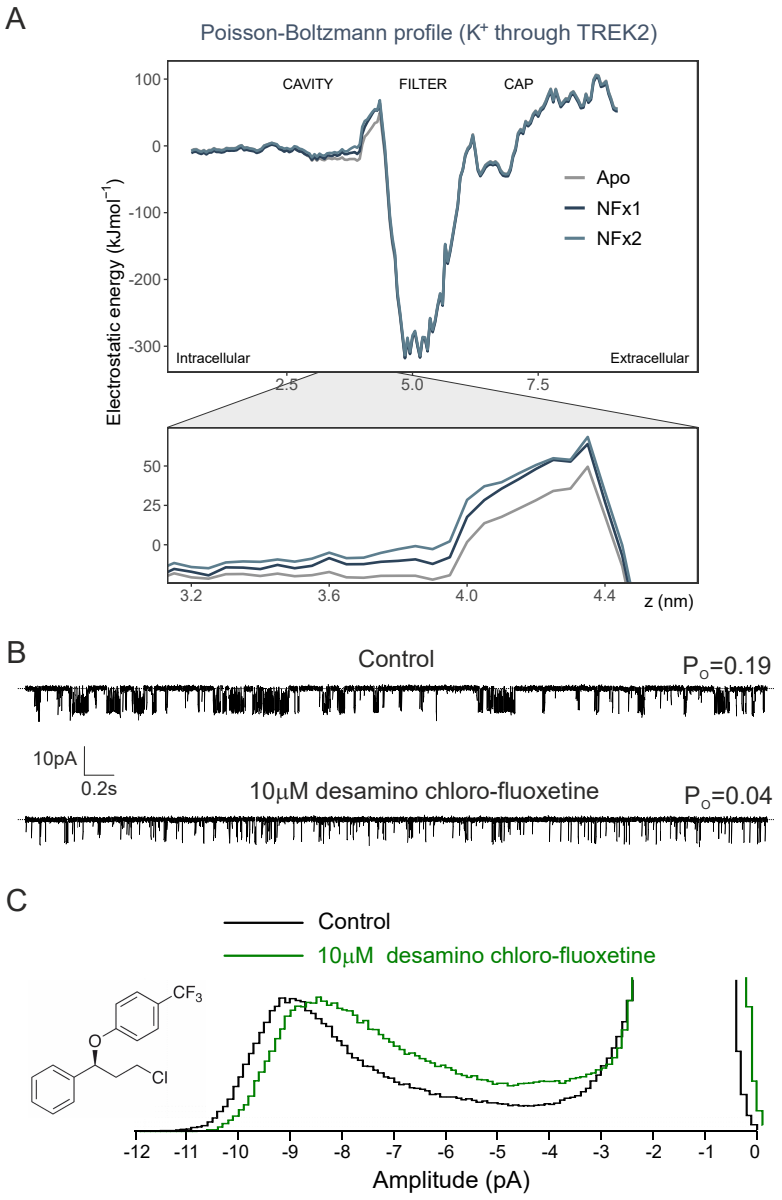

Proks et al. Supplementary Information

Notes on modelling

For the kinetic scheme in Figure 7C, mean open time (τ_O), mean short (τ_F) and long (τ_S) closed times and their corresponding areas A_F and A_S can be calculated from the following equations:

$$\tau_O = \frac{1 + (a_{12}/a_{21}) + a_{12}a_{23}/(a_{32}/a_{21})}{b_1 + (a_{12}/a_{21})b_2 + (a_{12}a_{23}/(a_{32}/a_{21}))\,b_3} \qquad \text{eq S1}$$

$$\tau_F = -\left(\frac{1}{4}\left(b_{-3}+d_3+d_{-3}+\sqrt{-4\,b_{-3}\,d_{-3}+(b_{-3}+d_3+d_{-3})^2}\right)^2\right)\left[\left(\frac{1}{4}\left(b_{-2}+d_2+d_{-2}+\sqrt{-4\,b_{-2}d_{-2}+(b_{-2}+d_2+d_{-2})^2}\right)^2 + \frac{a_{12}\,a_{23}\,b_3\,b_{-3}\left(b_{-3}+d_3-d_{-3}+\sqrt{(b_{-3}+d_3)^2+2(-b_{-3}+d_3)\,d_{-3}+d_{-3}^2}\right)}{2(a_{21}a_{32}b_1+a_{12}a_{32}b_2+a_{12}a_{23}b_3)\sqrt{b_{-3}^2+2b_{-3}(d_3-d_{-3})+(d_3+d_{-3})^2}}\right)\left[\left(\frac{1}{4}\left(b_{-1}+d_1+d_{-1}+\sqrt{-4\,b_{-1}\,d_{-1}+(b_{-1}+d_1+d_{-1})^2}\right)^2 + \frac{a_{12}\,a_{32}\,b_2\,b_{-2}\left(b_{-2}+d_2-d_{-2}+\sqrt{(b_{-2}+d_2)^2+2(-b_{-2}+d_2)\,d_{-2}+d_{-2}^2}\right)}{2(a_{12}a_{32}b_1+a_{12}a_{32}b_2+a_{12}a_{23}b_3)\sqrt{b_{-2}^2+2b_{-2}(d_2-d_{-2})+(d_2+d_{-2})^2}}\right)\left[\frac{a_{21}a_{32}\,b_1\,b_{-1}\left(b_{-1}+d_1-d_{-1}+\sqrt{(b_{-1}+d_1)^2+2(-b_{-1}+d_1)d_{-1}+d_{-1}^2}\right)}{2(a_{21}a_{32}b_1+a_{12}a_{32}\,b_2+a_{12}a_{23}b_3)\sqrt{b_{-1}^2+2b_{-1}(d_1-d_{-1})+(d_1+d_{-1})^2}}\right]\right]\right] \qquad \text{eq S2}$$

$$\tau_S = -\left(\frac{1}{4}\left(b_{-3}+d_3+d_{-3}-\sqrt{-4\,b_{-3}d_{-3}+(b_{-3}+d_3+d_{-3})^2}\right)^2\right)\left[\left(\frac{1}{4}\left(b_{-2}+d_2+d_{-2}-\sqrt{-4\,b_{-2}d_{-2}+(b_{-2}+d_2+d_{-2})^2}\right)^2 + \frac{a_{12}\,a_{23}\,b_3\,b_{-3}\left(b_{-3}+d_3-d_{-3}+\sqrt{(b_{-3}+d_3)^2+2\,(-b_{-3}+d_3)\,d_{-3}+d_{-3}^2}\right)}{2(a_{21}a_{32}b_1+a_{12}a_{32}b_2+a_{12}a_{23}b_3)\sqrt{b_{-3}^2+2\,b_{-3}(d_3-d_{-3})+(d_3+d_{-3})^2}}\right)\left[\left(\frac{1}{4}\left(b_{-1}+d_1+d_{-1}-\sqrt{-4\,b_{-1}d_{-1}+(b_{-1}+d_1+d_{-1})^2}\right)^2 + \frac{a_{12}\,a_{32}\,b_2\,b_{-2}\left(-b_{-2}-d_2+d_{-2}+\sqrt{(b_{-2}+d_2)^2+2(-b_{-2}+d_2)\,d_{-2}+d_{-2}^2}\right)}{2(a_{21}a_{32}b_1+a_{12}a_{32}b_2+a_{12}a_{23}b_3)\sqrt{b_{-2}^2+2\,b_{-2}\,(d_2-d_{-2})+(d_2+d_{-2})^2}}\right)\left[\frac{a_{21}a_{32}\,b_1\,b_{-1}\left(-b_{-1}-d_1+d_{-1}+\sqrt{(b_{-1}+d_1)^2+2\,(-b_{-1}+d_1)\,d_{-1}+d_{-1}^2}\right)}{2(a_{21}a_{32}b_1+a_{12}\,a_{32}\,b_2+a_{12}a_{23}b_3)\sqrt{b_{-1}^2+2\,b_{-1}(d_1-d_{-1})+(d_1+d_{-1})^2}}\right]\right]\right] \qquad \text{eq S3}$$

$$A_F = -\left(\frac{1}{4}\left(b_{-3}+d_3+d_{-3}+\sqrt{-4\,b_{-3}d_{-3}+(b_{-3}+d_3+d_{-3})^2}\right)^2\right)\left[\left(\frac{1}{2}\left(-b_{-2}-d_2-d_{-2}-\sqrt{-4\,b_{-2}d_{-2}+(b_{-2}+d_2+d_{-2})^2}\right) + \frac{a_{12}a_{23}b_3b_{-3}\left(b_{-3}+d_3-d_{-3}+\sqrt{(b_{-3}+d_3)^2+2\,(-b_{-3}+d_3)\,d_{-3}+d_{-3}^2}\right)}{2(a_{21}a_{32}b_1+a_{12}a_{32}b_2+a_{12}a_{23}b_3)\sqrt{b_{-3}^2+2\,b_{-3}(d_3-d_{-3})+(d_3+d_{-3})^2}}\right)\left[\left(\frac{1}{2}\left(-b_{-1}-d_1-d_{-1}-\sqrt{-4\,b_{-1}d_{-1}+(b_{-1}+d_1+d_{-1})^2}\right) + \frac{a_{12}a_{32}b_2b_{-2}\left(b_{-2}+d_2-d_{-2}+\sqrt{(b_{-2}+d_2)^2+2(-b_{-2}+d_2)\,d_{-2}+d_{-2}^2}\right)}{2(a_{21}a_{32}b_1+a_{12}a_{32}b_2+a_{12}a_{23}b_3)\sqrt{b_{-2}^2+2\,b_{-2}(d_2-d_{-2})+(d_2+d_{-2})^2}}\right)\left[\frac{a_{21}a_{32}b_1b_{-1}\left(b_{-1}+d_1-d_{-1}+\sqrt{(b_{-1}+d_1)^2+2(-b_{-1}+d_1)\,d_{-1}+d_{-1}^2}\right)}{2(a_{21}a_{32}b_1+a_{12}a_{32}b_2+a_{12}a_{23}b_3)\sqrt{b_{-1}^2+2\,b_{-1}(d_1-d_{-1})+(d_1+d_{-1})^2}}\right]\right]\right] \qquad \text{eq S4}$$

$$A_S = -\left(\frac{1}{4}\left(b_{-3}+d_3+d_{-3}-\sqrt{-4\,b_{-3}\,d_{-3}+(b_{-3}+d_3+d_{-3})^2}\right)^2\right)\left[\left(\frac{1}{2}\left(-b_{-2}-d_2-d_{-2}+\sqrt{-4\,b_{-2}d_{-2}+(b_{-2}+d_2+d_{-2})^2}\right) + \frac{a_{12}a_{23}b_3b_{-3}\left(-b_{-3}-d_3+d_{-3}+\sqrt{(b_{-3}+d_3)^2+2\,(-b_{-3}+d_3)\,d_{-3}+d_{-3}^2}\right)}{2\,(a_{21}a_{32}b_1+a_{12}\,a_{32}\,b_2+a_{12}a_{23}b_3)\,\sqrt{b_{-3}^2+2\,b_{-3}(d_3-d_{-3})+(d_3+d_{-3})^2}}\right)\left[\left(\frac{1}{2}\left(-b_{-1}-d_1-d_{-1}+\sqrt{-4\,b_{-1}d_{-1}+(b_{-1}+d_1+d_{-1})^2}\right) + \frac{a_{12}a_{32}b_2b_{-2}\left(-b_{-2}-d_2+d_{-2}+\sqrt{(b_{-2}+d_2)^2+2\,(-b_{-2}+d_2)\,d_{-2}+d_{-2}^2}\right)}{2\,(a_{21}a_{32}b_1+a_{12}\,a_{32}\,b_2+a_{12}a_{23}b_3)\,\sqrt{b_{-2}^2+2\,b_{-2}(d_2-d_{-2})+(d_2+d_{-2})^2}}\right)\left[\frac{a_{21}a_{32}\,b_1\,b_{-1}\left(-b_{-1}-d_1+d_{-1}+\sqrt{(b_{-1}+d_1)^2+2\,(-b_{-1}+d_1)\,d_{-1}+d_{-1}^2}\right)}{2\,(a_{21}a_{32}\,b_1+a_{12}\,a_{32}\,b_2+\,a_{12}a_{23}b_3)\sqrt{b_{-1}^2+2\,b_{-1}(d_1-d_{-1})+(d_1+d_{-1})^2}}\right]\right]\right] \qquad \text{eq S5}$$

Each rate constant in the kinetic scheme in Fig 7c is a function of voltage, i.e:

$$a_{ij} = A_{ij}e^{\frac{\alpha_{ij}FV}{RT}} \quad \text{eq S6}$$

$$b_i = B_i e^{\frac{\beta_i FV}{RT}} \quad \text{eq S7}$$

$$b_{-i} = B_{-i}e^{\frac{\beta_{-i}FV}{RT}} \quad \text{eq S8}$$

$$d_i = D_i e^{\frac{\delta_i FV}{RT}} \quad \text{eq S9}$$

$$d_{-i} = D_{-i}e^{\frac{\delta_{-i}FV}{RT}} \quad \text{eq S10}$$

where indexes $1 \leq i,j \leq 3$, V is the membrane voltage, F is the Faraday constant, R is the gas constant and T is the temperature. Equations S1-S10 could be fit directly to the parameters of open and closed time distributions with the mean open time corrected for missed events.

Below -40mV, the data was best fit with a linear scheme O_1-C_{F1}-C_{S1} which forms the left part of the scheme in Fig 10C with the following parameters:

B_1 = 1.98ms^{-1} B_{-1}= 24ms^{-1}

β_1 = -0.34 β_{-1} = 0.25

D_1 = 1.55 ms^{-1} D_{-1} = 0.89ms^{-1}

δ_1 = 0.53 δ_{-1}= -0.17

Voltage dependence of data between -40mV and +60mV was possible to reproduced by adding states O_2-C_{F2}-C_{S2} with a connection between the two open states (connecting new states via closed states produced greater errors in fits). Finally, another set of three states O_3-C_{F3}-C_{S3} was necessary to add in order account for changes in voltage-dependence of open times and areas of closed times above +60mV. Models created by connecting various combinations of O-C_F-C_S and C_F-O-C_S states produced either poor fits of data of failed to converge to a solution.

Analysis of the data with the kinetic scheme in Fig 7C revealed that there are many possible solutions which fit the data with similar accuracy with wide ranging values particularly for constants A_{ij} and α_{ij}. One of the solutions is shown in Fig S5; the corresponding voltage dependence of the mean open and closed time distribution parameters is shown in Fig 7D-G where the lines are drawn using the model components in Fig S5 according to the following equations:

$$\tau_O = \tau_{O1}A_{O1} + \tau_{O2}A_{O2} + \tau_{O3}A_{O3} \quad \text{eq S11}$$

$$\tau_F = \frac{\tau_{C1}A_{C1}+\tau_{C3}A_{C3}+\tau_{C5}A_{C5}}{A_{C1}+A_{C3}+A_{C5}} \quad \text{eq S12}$$

$$\tau_S = \frac{\tau_{C2}A_{C2}+\tau_{C4}A_{C4}+\tau_{C6}A_{C6}}{A_{C2}+A_{C4}+A_{C6}} \quad \text{eq S13}$$

$$A_F = A_{C1} + A_{C3} + A_{C5} \quad \text{eq S14}$$

$$A_S = A_{C2} + A_{C4} + A_{C6} \quad \text{eq S15}$$

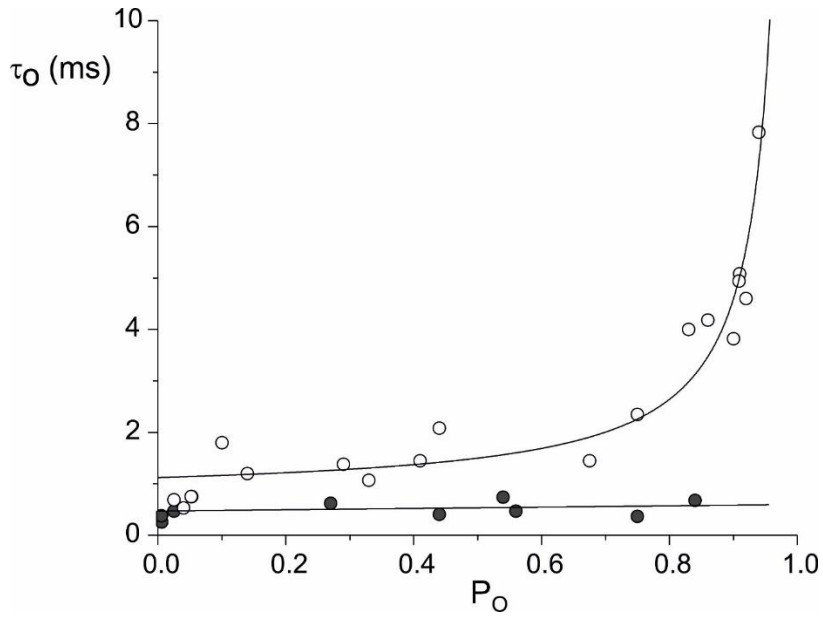

Supplementary Figure S1. The relationship between P_O and mean open time τ_0. Data were obtained from single-channel recordings of TREK-2 at +60mV (open circles) and -60mV (filled circles). Lines are drawn by hand.

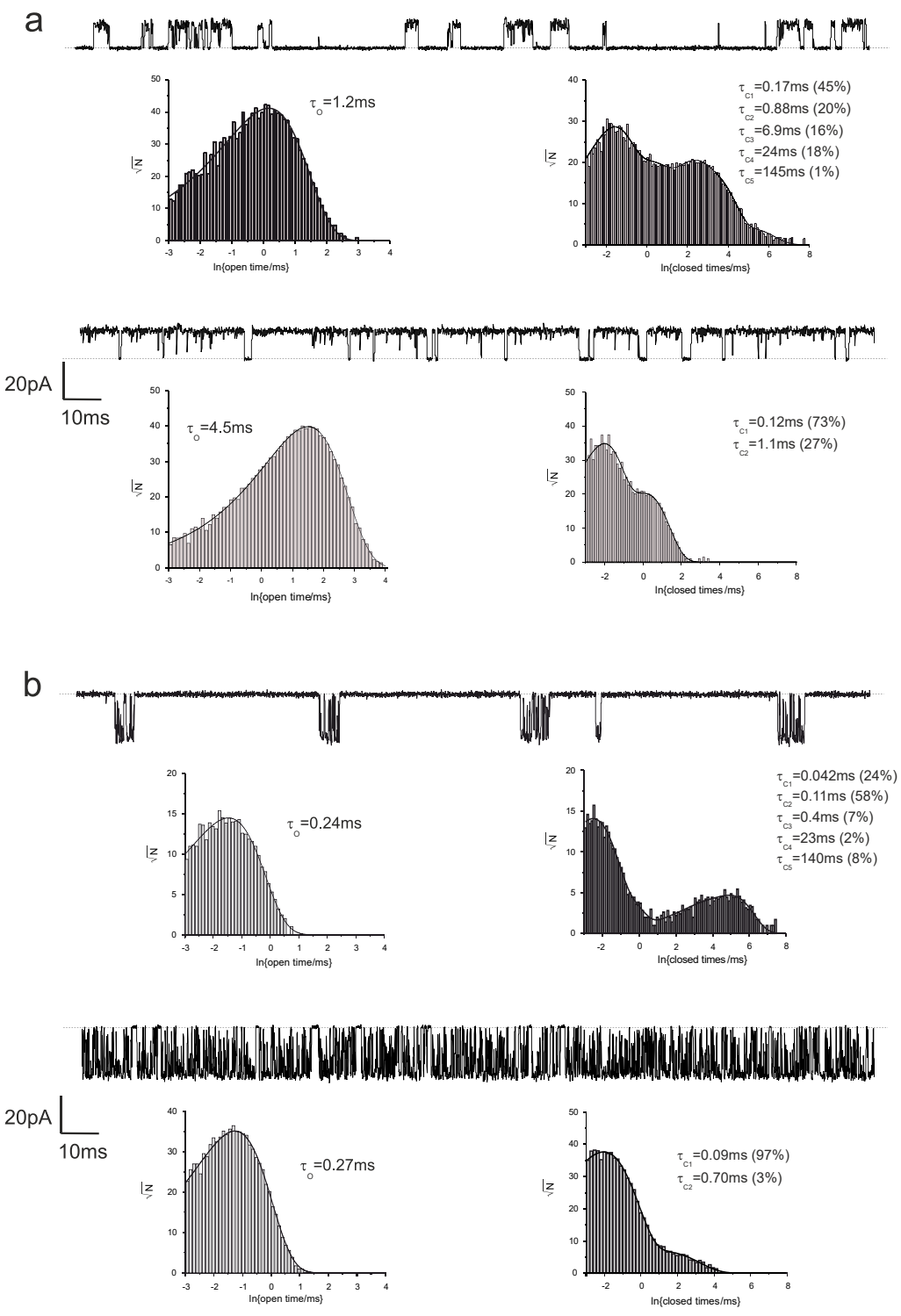

<u>Supplementary Figure S2:</u> Comparison of single channel kinetics of TREK channels in standard and high P_O mode. Representative examples of outward (a) and inward (b) TREK-2 single channel currents. in standard (a) and high P_O mode (b). a. Top traces: single-channel recordings of TREK-2 in standard (top trace, P_O =0.14) and high P_O mode (bottom trace, P_O =0.92) at +80mV. Dotted line represents the closed channel level. Bottom panels: distributions of single-channel openings (left) and closures (right) obtained from recordings of TREK-2 in standard and "high P_O" mode at +80mV. **b.** Top traces: single-channel recordings of TREK-2 in standard (top trace, P_O =0.013) and "high P_O" mode (bottom trace, P_O =0.70) at -80mV. Dotted line represents the closed channel level. Bottom panels: distributions of single-channel openings (left) and closures (right) obtained from recordings of TREK-2 in standard and "high P_O" mode at -80mV.

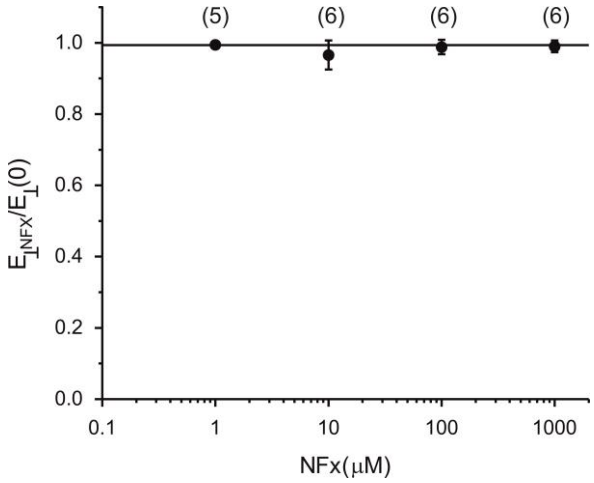

Supplementary Figure S3. Effects of NFx on the physical properties of the membrane. The relationship between the modulus of elasticity in the perpendicular direction of the membrane in the presence of norfluoxetine ($E_{\perp NFX}$), normalized to that in control solution ($E_{\perp}(0)$). Number of experimental values are shown above each point. The line is fit by hand.

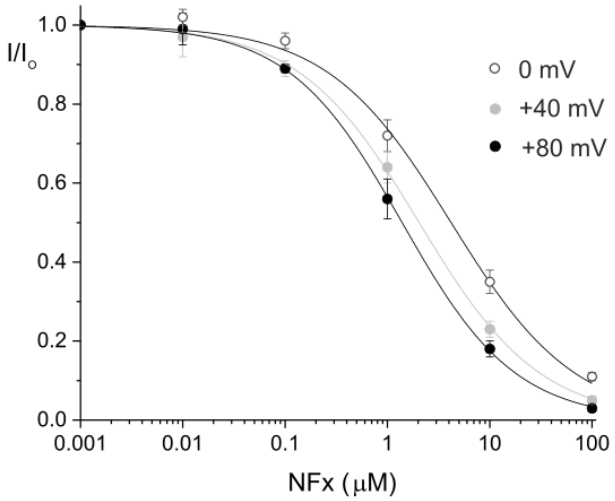

Supplementary Figure S4. Voltage-dependence of NFx block at depolarized potentials. Dose-response relationships were determined at different voltages for NFx inhibition of macroscopic currents in giant excised patches from oocytes expressing WT TREK-2. At saturating concentrations, relatively little voltage-dependence is observed but at depolarized potentials a small shift is observed. The lines are fit with a Hill inhibition equation. The IC_{50} values are: 4.2 μM, h=0.72 (0 mV); 2.0 μM h=0.74 (+40mV); and 1.4 μM h=0.79 (+80mV).

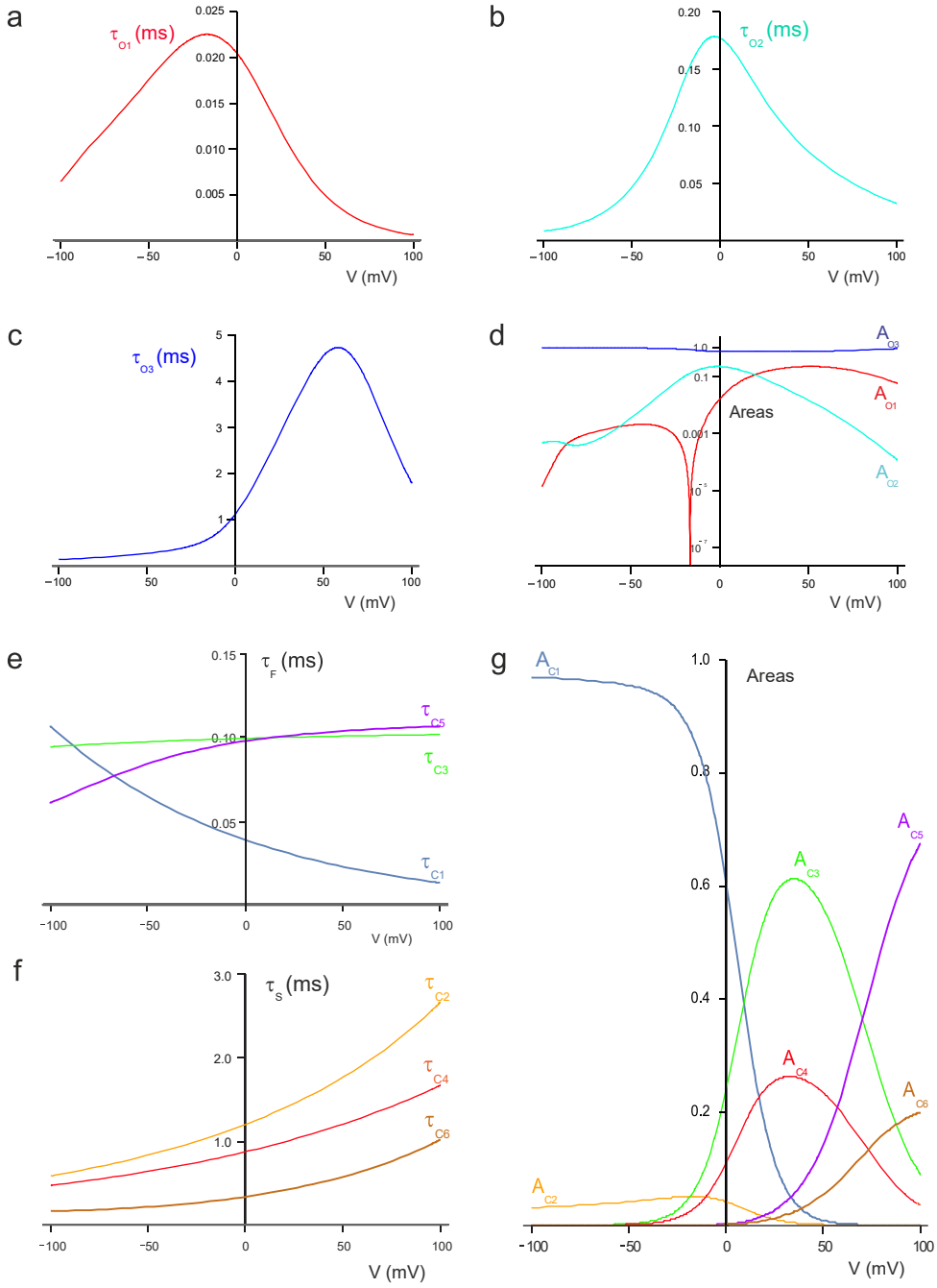

<u>Supplementary Figure S5.</u> Properties of open and closed times of the kinetic model of TREK-2 selectivity filter gate. a-d. Voltage dependence of lifetimes **(a-c)** and relative areas **(d)** of open states of the kinetic model depicted in Figure 7C. **e-g.** Voltage dependence of short **(e),** long **(f)** closed states and relative areas **(g)** of the of the kinetic model depicted in Figure 10C. The following parameters were used in the model: A_{12}=5ms^{-1}, A_{21}=20 ms^{-1}, α_{12}=0.46, α_{21}=-0.46, A_{23}=21 ms^{-1}, α_{23}=0.95, A_{32}=3.5 ms^{-1}, α_{32}=-0.95, B_2=4.2ms^{-1}, β_2=1.3, B_{-2}=7.2 ms^{-1}, β_{-2}=1.6*10^{-5}, B_3=6.2*10^{-3}ms^{-1}, β_3=1.1, B_{-3}=7.5, β_{-3}= 2.1*10^{-5}, D_2=2.4, δ_2 =1.2*10^{-5}, D_{-2}=1.6 δ_{-2}=-0.17, D_3=1.7ms^{-1}, δ_3=6.4*10^{-5}, D_{-3}=4ms^{-1}, δ_{-3}=-0.30.

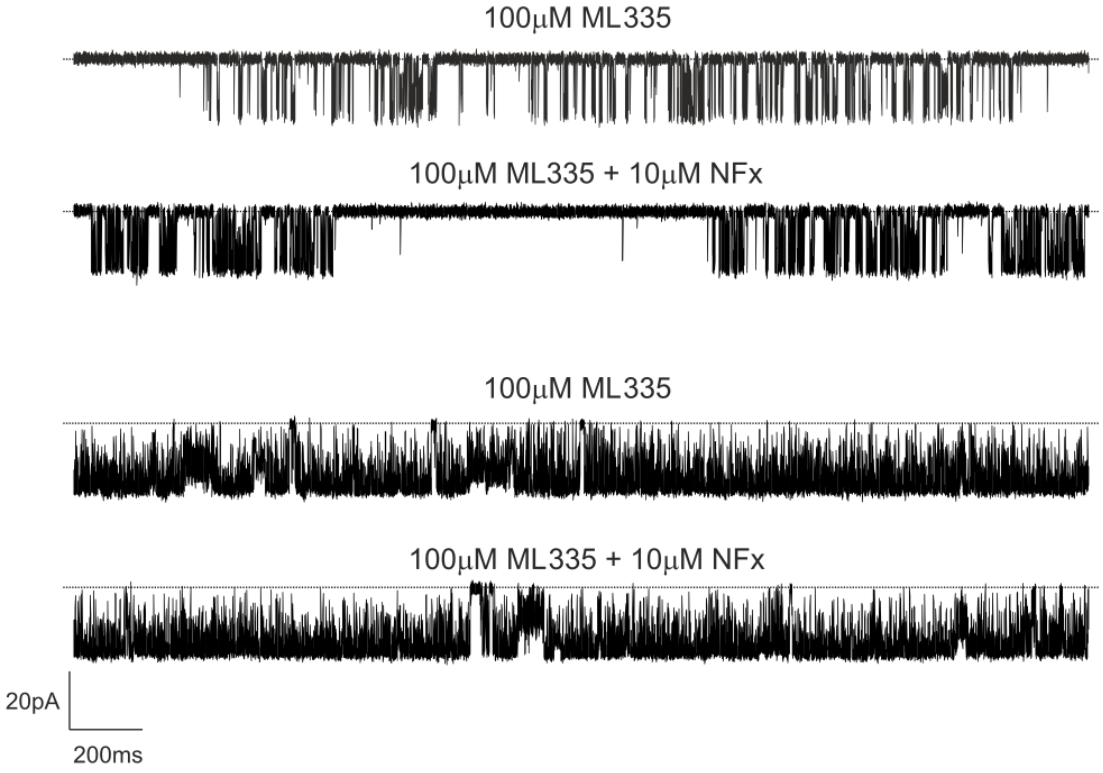

Supplementary Figure S6. Norfluoxetine effects on single TREK-2 channel properties are abolished in the presence of 100μM ML335. Examples of single-channel recordings of TREK-2 channels at -40mV in excised patched from HEK 293 cells in the presence of 100μM ML335 having either partial (**top two traces**) or maximal (**bottom two traces**) effect on single-channel open probability either in the absence or presence of 10μM NFx, as indicated. Dotted lines in top traces represent the closed channel level. Note that NFx has no effect on either P_o or γ in the presence of ML335.